

Grid Integration of a Dual Two-Level Voltage-Source Inverter Considering Grid Impedance and Phase-Locked Loop

Amir Aghazadeh¹, Masoud Davari¹, *Senior Member, IEEE*, Hamed Nafisi¹,
and Frede Blaabjerg², *Fellow, IEEE*

Abstract—This article proposes a dual two-level voltage-source inverter (DTL VSI) and its control to effectively integrate two dc sources into the multi-infeed ac/dc (MIACDC) power architecture of fully integrated power and energy systems (FIPESs). The current-controlled method is also synthesized and proposed to control the grid-connected DTL VSI. To this end, this article provides mathematical analyses comparing the DTL VSI with the conventional current-controlled grid-connected two-level VSIs (TL VSIs). The linearized state-space models of both systems are mathematically derived for analyzing the dynamics of both structures. These models reveal the salient feature of the proposed DTL VSIs used in grid integration. To this end, space-phasor analysis is employed, and the dynamics of the phase-locked loop (PLL) and the grid impedance are also considered. The proposed grid-connected DTL VSI (with the current-controlled algorithm) not only in weak grids (for normal grid conditions) but even after fault removal (for faulty grid conditions) stabilizes the active and reactive power dynamics with improved transient performance compared with that of its conventional counterpart. Therefore, it enhances the operation range of the VSIs integrating various entities in FIPES' MIACDC power architecture. This article provides supportive simulation results and experiments generated by MATLAB and a scaled-down test rig, respectively.

Index Terms—Dual two-level voltage-source inverter (DTL VSI), phase-locked loop (PLL) dynamics, space-phasor vector control, two-level voltage-source inverter (TL VSI), voltage-source inverter (VSI), weak grids.

I. INTRODUCTION

DU^E to the significant amount of green gas emitted by human beings, and by considering its irrecoverable

Manuscript received June 10, 2019; revised August 4, 2019 and September 28, 2019; accepted October 23, 2019. Date of publication November 14, 2019; date of current version January 20, 2021. This work was supported by the U.S. National Science Foundation (NSF) through ECCS-EPCN under Grant 1902787 and Grant 1808279, and it has been done entirely at Georgia Southern University (Statesboro Campus). Recommended for publication by Associate Editor Suryanarayana Doolla. (Corresponding author: *Masoud Davari*.)

A. Aghazadeh and H. Nafisi are with the Center of Excellence in Power Systems, Department of Electrical Engineering, Amirkabir University of Technology, Tehran 15914, Iran (e-mail: amir_aaghazadeh@aut.ac.ir; nafisi@aut.ac.ir).

M. Davari is with the Department of Electrical and Computer Engineering, Georgia Southern University (Statesboro Campus), Statesboro, GA 30460 USA (e-mail: mdavari@georgiasouthern.edu; davari@ualberta.ca).

F. Blaabjerg is with the Department of Energy Technology, Aalborg University, DK-9220 Aalborg, Denmark (e-mail: fbl@et.aau.dk).

Color versions of one or more of the figures in this article are available online at <https://ieeexplore.ieee.org>.

Digital Object Identifier 10.1109/JESTPE.2019.2953522

effects on the environment, many countries adopt renewables as an alternative to fossil fuels. Therefore, the energy sector has been significantly progressing and moving toward integrating power networks and energy storage systems, which forms the fully integrated power and energy systems (FIPESs). Energy storage systems will be mostly in the form of battery systems embedded in ac/dc grids. FIPESs use multi-infeed ac/dc (MIACDC) power systems. MIACDC simpler versions are found in super grids and meshed high-voltage direct current grids—in transmission systems—and hybrid multiterminal ac/dc grids—in both distribution systems and modernized microgrids (MMGs) [1]. They have been employed in smart grids nowadays. In smart grids, the upgraded MIACDC concept brings many benefits to the operation, control, and demand and supply within commercial power systems.

Due to the essential advances brought to the field of power electronics and semiconductor devices, different types of inverters are employed to connect renewables and sources to MIACDC power architecture of FIPESs [2]–[8]. Among different structures of voltage-source inverters (VSIs), dual two-level VSIs (DTL VSIs) are well known due to its significant advantages brought in motor and drive controls (e.g., voltage total harmonic distortion (THD), voltage-weighted THD, and switching losses) [9], [10].

The DTL VSI can be one of the up-and-coming power electronic topologies—which is employed in the FIPESs of MMGs. DTL VSIs empower an FIPES to be able to benefit from the MIACDC power systems' architecture. DTL VSI can be implemented by either a single dc source or two separate dc sources. Nonetheless, DTL VSI with two dc sources benefits from lower voltage and current THD, lack of circulating currents, and two isolated paths for transferring power to the power grid [9], [10]. The lower voltage and current THDs lead to a decrease in the cost of installation and maintenance decreases. Additionally, by utilizing two separate paths, the reliability of the system is augmented since, in case of missing one of the paths, another path is still able to transfer a portion of power. In comparison with systems containing single VSIs, DTL VSI provides some substantial benefits. For instance, with the given nominal power, this structure reduces the total manufacturing and installation cost [11]. Furthermore, DTL VSIs benefit from a higher magnitude of the output voltage with the same amount of dc-link voltage compared with VSI. This advantage reduces the turn ratio and

output impedance of the transformer needed to step up the output voltage of the DTL VSI. Besides, the reliability of the system employing DTL VSI is improved because of using two paths of power supply. Therefore, inverters based on dual configurations attract more attention, and they are commonly utilized in grid-connected photovoltaic systems [11]–[14].

DTL VSIs have been mainly employed in motor and drive controls so far. If DTL VSI is used in grid integration applications, its current benefits (elaborated in [2]–[14]) will be add-ons to the grids into which integrated. One fundamental example of those grids is the power network based on MIACDC architectures. Also, a significant amount of effort has been put to assess the stability of grid-connected, PQ-controlled VSIs under different grid conditions [15]–[29]. However, to the best of our knowledge, the stability assessment of the grid-connected DTL VSI at a wide range of short-circuit capacity ratios (SCCRs) has not indeed and technically investigated yet. Based on these pieces of information, the contributions of this article have been listed as follows.

- 1) The grid-connected DTL VSI is proposed in order to be utilized as a single PQ-controlled VSI integrating two separated dc sources, which enhances the MIACDC's grid integration effectively.
- 2) A simple, yet powerful current control algorithm is proposed for the PQ-controlled VSI.
- 3) The impacts of the grid weakness causing the instability, controller parameters, and the dynamics of the phase-locked loop (PLL) regardless of its type (see [19], [20]) on the stability of grid-connected VSIs are addressed in [23] and [27]–[29]. The proposed grid-connected DTL VSI and its performance at different SCCR and in normal and faulty grid conditions are comprehensively evaluated and demonstrate the significant improvement in MIACDC's grid integration.
- 4) Based on the small-signal stability and eigenvalue analyses, the stability of the grid integration using grid-connected DTL VSIs is improved compared with that of conventional VSIs.
- 5) This article also reveals the key factors (including stability boundaries) affecting the stability of the closed-loop dynamic system formed by the proposed grid-connected DTL VSI. The provided stability analysis aims to assess the stability of the grid-connected DTL VSI and TL VSI at different SCCR when X_S/R_S equals to one (to have the worst case [26]), and the parameters of the PLL are constant.
- 6) It will be demonstrated that a grid-connected DTL VSI is able to enhance the integration of new upcoming dc power sources into MIACDC power systems effectively. As regards this, at different SCCR and in normal and fault conditions, both converters have been analyzed, simulated, and experimentally tested. The results reveal that the proposed grid-connected DTL VSI is able to achieve a more extensive stable range of performance, compared to grid-connected VSIs, while having better and acceptable THD, power quality, and losses.

The remainder of this article has been structured as follows. The system description of the grid-connected of DTL VSIs is

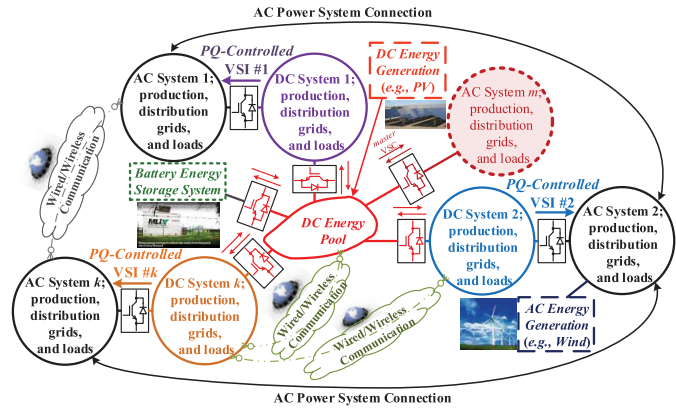


Fig. 1. Notional structure of an MIACDC power architecture.

shown in Section II. In Section III, the small-signal model and eigenvalue studies of the DTL VSIs are provided and compared with those of TL VSIs. Sections IV and V demonstrate the simulation results and experiments. Section VI finally concludes this article's outcomes.

II. SYSTEM DESCRIPTION OF GRID-CONNECTED DTL VSIs

A notional architecture of an MIACDC's power grid (both power and communication one) has been shown in Fig. 1. As shown in Fig. 1, many power electronic links should work as PQ-controlled inverters transferring power from the dc side to the ac side, e.g., VSI #1, VSI #2, and VSI #k in Fig. 1.

A. Configuration

The DTL VSI connected to an MIACDC grid is shown in Fig. 2, where each inverter is separately supplied by one dc source. In order to eliminate the generated harmonic contents at the output voltage of the DTL VSI, one *LC*-filter is installed. The inductance of this filter has been shown in Fig. 2 for each VSI constituting the DTL VSI; the capacitance of the aforementioned filter is C —shown in Fig. 2. In order to consider the resistance of the filter and that of the switch ON-state, thereby increasing the accuracy of the model, a resistor is added to the system and termed by R , which represents the sum of the resistance of each coil of the filter and that of the switch ON-state (described by r_{on} in [19] and [30]). A PLL is connected through C (referred to Fig. 2, the voltage between \vec{v}_{PCC}^+ and \vec{v}_{PCC}^- is named \vec{v}_{PCC}) to obtain the angle of \vec{v}_{PCC} , termed ρ , to synchronize the DTL VSI with the grid.

B. Principle of Operation

As shown in Fig. 2, DTL VSI contains two conventional VSIs adjusting active and reactive powers at the point of common coupling (PCC). Therefore, based on the space-phasor control method (i.e., vector control algorithm), the output voltage of DTL VSI (i.e., the voltage between a and a' , b and b' , and c and c') has to be controlled; their corresponding space phasors are $+\vec{v}_{PCC}$ and $-\vec{v}_{PCC}$. An ac-side filter is employed to eliminate the switching voltage harmonics. However, since

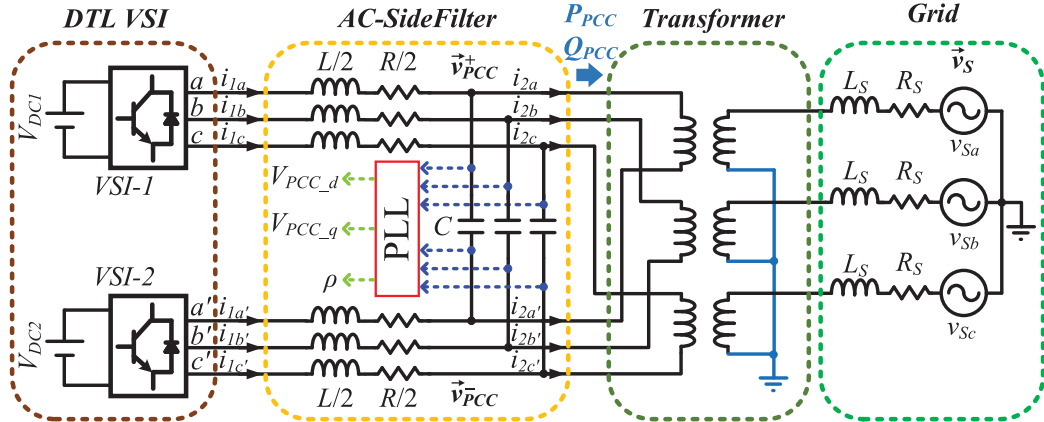


Fig. 2. PQ-controlled, grid-connected DTL VSI used in the MIACDC power grids.

both VSIs generate voltage harmonics, two similar inductive filters have been used for each VSI. The capacitor of the filters, as can be seen, is connected between two pairs of three phases. It is noteworthy that for connecting DTL VSI to the grid, an open-ended transformer has to be employed because the number of output phases of DTL VSI is six. Nevertheless, the power network consists of three phases. While each winding of the primary side is connected between two analogous phases of each TL VSI (e.g., between a and a'), the windings of the secondary side are connected in star, i.e., in "Y" configuration. In order to achieve the highest output voltage, as well as reduced harmonic contents in the output voltage of DTL VSI, the two VSIs of the DTL VSI should work with a 180° phase difference between their reference voltages [9], [10]. Consequently, the three reference voltages of VSI-1 are kept stationary, and the reference voltages of VSI-2 are shifted by 180° . Therefore, as soon as the reference voltages are generated and applied to VSI-1, these signals are shifted by 180° and used in VSI-2; a phase shifter, named "180° phase shifter" in Fig. 4, is employed to provide appropriate reference voltages for both VSIs. Furthermore, the switching pulses of each VSI are generated by a conventional sinusoidal pulsewidth modulation (SPWM) technique.

Fig. 3 shows the principle of operation of a PQ-controlled DTL VSI. In Fig. 3, using the controller proposed in Section II-B (i.e., Fig. 4; DTL VSI has undergone active power and reactive power changes, whose illustrative waveforms shown. In Fig. 3, 100% increase in active power and reactive power reference signals has been applied at $t = 1.5$ s and $t = 2.5$ s, respectively, while the DTL VSI's operating point is 10 kW/10 kvar for $t < 1.5$ s. Fig. 3 has demonstrated P_{PCC} and Q_{PCC} ; the magnitude and phase of space phasors \vec{v}_{PCC} and \vec{v}_S ; different phase currents; and all of the modulation indices shown in Fig. 2—the data used for generating results of Fig. 3 have been reported through Table III in the Appendix using $\text{SCCR} = 10$. As stated, the modulations indices of phases a' , b' , and c' are the 180° shifted modulations indices of phases a , b , and c .

C. Proposed Control Structure

In this article, the current-controlled method is proposed for controlling the active power and reactive power of the

PQ-controlled DTL VSI, which benefits from feedforward controls. It has been shown in Fig. 4, where $V_{\text{PCC_dn}}$ is d -axis of the nominal voltage value at PCC. By employing this method, the inner control loops are responsible for adjusting the DTL VSI output currents by controlling the DTL VSI voltage in the d - and q -axes. For any control loops, based on the internal model principle in the classical control theory, proportional-integral (PIs) controllers are employed. Here, to control active power and reactive power, the d -axis current and q -axis current are controlled according to the representation of the current space phasor in the dq -frame [30]. Also, in order to enhance the performance of the current controller, two feedforward signals of the d - and q -axes of \vec{v}_{PCC} are included; the time constant of the utilized filters is T .

D. Power Network

As shown in Fig. 2, the grid is modeled using its Thévenin's equivalent circuit consisting of an ideal voltage, L_S , and R_S . Note that the amplitude of the voltage source is the same as the grid nominal voltage. To determine the values of passive components, the short circuit capacity (SCC) at PCC is derived using $\text{SCC}_{\text{PCC}} = \text{SCCR} \times S_{\text{VSI}}$, where S_{VSI} is the nominal power of the inverter connected to the grid, and in this article, $S_{\text{VSI}} = S_{\text{DTL VSI}} = S_{\text{TL VSI}}$. After calculating SCC_{PCC} , the Thévenin model impedance is derived based on $Z = (V_{\text{PCC_rms}}^2 / \text{SCC}_{\text{PCC}})$, where $V_{\text{PCC_rms}}^2$ is the rms value of the line-to-line nominal voltage at PCC. Finally, based on the assumptions mentioned in Section I, R_S and L_S are determined as $R_S = Z / \sqrt{2}$ and $L_S = Z / (2\pi f \sqrt{2})$, where f is the frequency of the grid in Hz.

III. EIGENVALUE ANALYSIS OF THE GRID-CONNECTED DTL VSIs

In order to evaluate grid-connected DTL VSIs and compare their performance with other commonly used VSIs' performance, the state-space model of the whole closed-loop system is required. In doing so, different parts of the system are considered, and their corresponding equations are derived. These parts include ac-side dynamics, control systems, and the PLL.

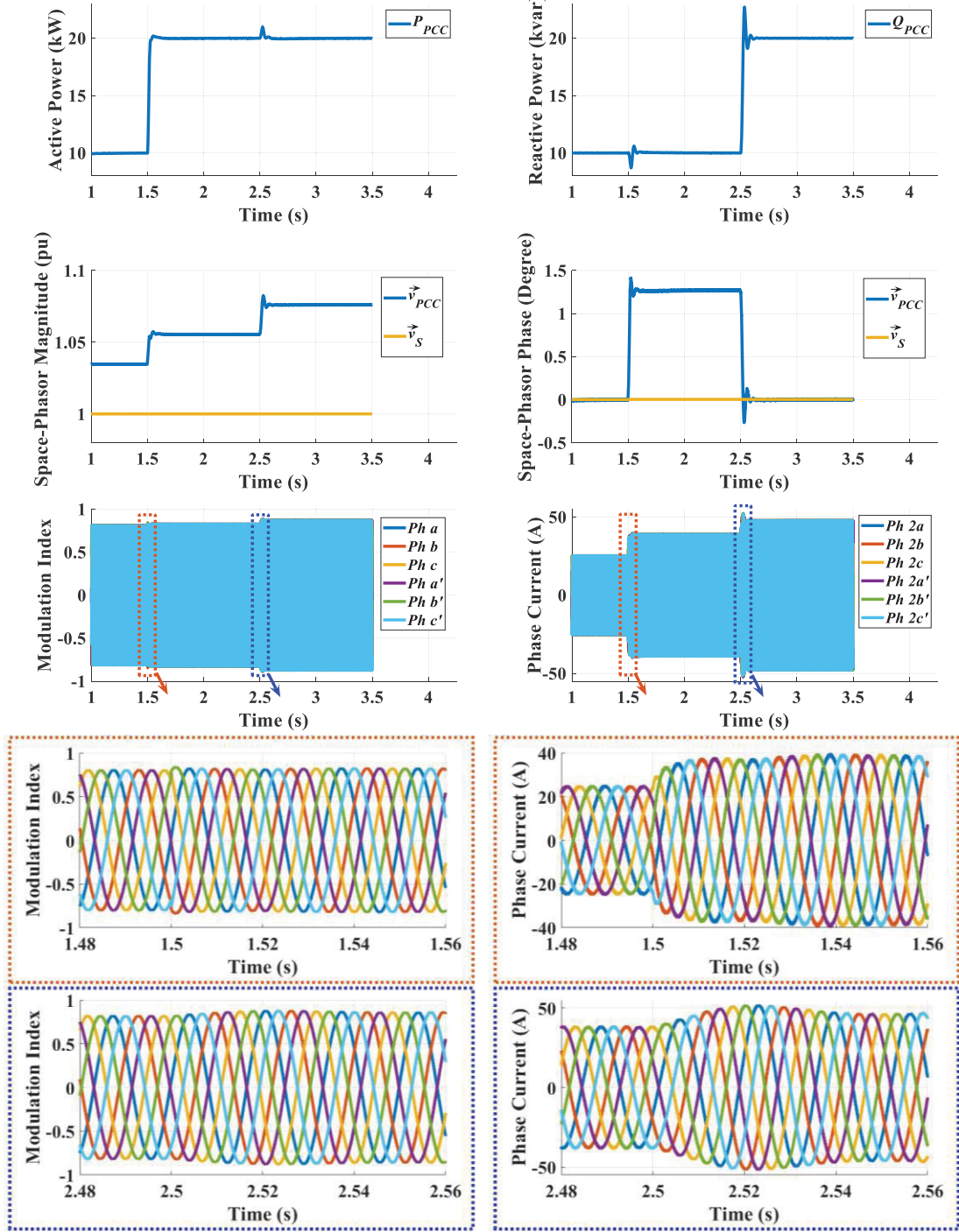


Fig. 3. PQ-controlled DTL VSI (using the controller proposed in Fig. 4), which has undergone active power and reactive power changes with illustrative waveforms showing the principle of operation.

A. AC-Side Dynamics in the dq -Frame

By employing the dq -frame representation of related space phasors [30], the dynamics of interest in the three-phase abc frame are transformed into the dq -frame. It should be pointed out that the voltage in the d -axis is in the in-phase with V_{PCC} . The dynamics of the grid-connected DTL VSI explained in Fig. 2 are formulated by (1)–(6) based on the equivalent circuit of the system. The equivalent circuit is shown in Fig. 5. In (1)–(6), subscripts d and q represent the quantities in the

d - and q -axes, and “1” and “2” show the currents of the inverter and grid sides, respectively. Besides, L , R , and C ; and L_S and R_S are the inductance, its resistance, and the capacitance of the related LC -filter; and the equivalent inductance and the equivalent resistance of the grid, respectively. It is noteworthy that since both converters of the DTL VSI work with the same modulation index (MI)—but with the 180° phase difference—the output voltages of each VSI in the dq -frame are $V_{t1d} = -V_{t2d} = V_{td}$ and

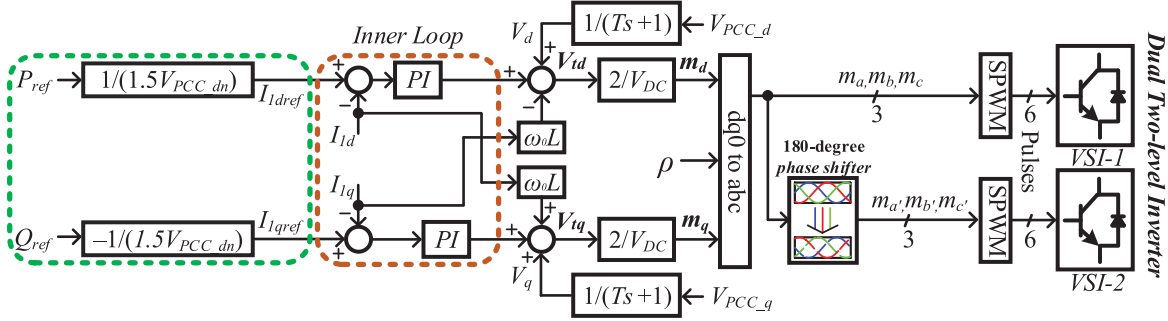


Fig. 4. Proposed control block diagram of the DTL VSI.

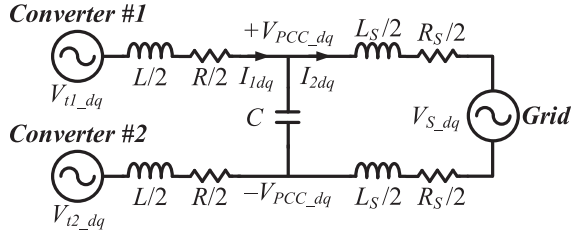


Fig. 5. Equivalent average model of the grid-connected DTL VSI.

$$V_{t1q} = -V_{t2q} = V_{tq}.$$

$$L \frac{dI_{1d}}{dt} = 2V_{td} - V_{pcc_d} + L\omega(t)I_{1q} - RI_{1d} \quad (1)$$

$$L \frac{dI_{1q}}{dt} = 2V_{tq} - V_{pcc_q} - L\omega(t)I_{1d} - RI_{1q} \quad (2)$$

$$L_S \frac{dI_{2d}}{dt} = V_{pcc_d} - V_{s_d} + L_S\omega(t)i_{2q} - R_S I_{2d} \quad (3)$$

$$L_S \frac{dI_{2q}}{dt} = V_{pcc_q} - V_{s_q} - L_S\omega(t)i_{2d} - R_S I_{2q} \quad (4)$$

$$C \frac{dV_{pcc_d}}{dt} = I_{1d} - I_{2d} + C\omega(t)V_{pcc_q} \quad (5)$$

$$C \frac{dV_{pcc_q}}{dt} = I_{1q} - I_{2q} - C\omega(t)V_{pcc_d} \quad (6)$$

where V_{s_d} is the d -component of the grid's Thévenin-equivalent voltage, V_{s_q} is the q -component of the grid's Thévenin-equivalent voltage, V_{td} is the d -component of the terminal voltage, V_{tq} is the q -component of the terminal voltage, V_{pcc_d} is the d -component of the PCC voltage (and V_d is its filtered signal using a filter with the time constant of T), V_{pcc_q} is the q -component of the PCC voltage (and V_q is its filtered signal using a filter with the time constant of T), I_{1d} is the d -component of the ac-side current of VSI-1, which is passing through the inductance L , I_{1q} is the q -component of the ac-side current of VSI-1, which is passing through the inductance L , I_{2d} is the d -component of the ac-side current of the grid, I_{2q} is the q -component of the ac-side current of the grid, L is the inductance of the filter, R is the sum of the resistance of the filter and that of the switch ON-state (r_{on} in [30]), C is the capacitance of the filter, L_S is the grid inductance, R_S is the grid resistance, and $\omega(t)$ is the angular frequency of the grid—all have been demonstrated in Figs. 2 and 5.

It is noteworthy that (1)–(6) describe the dynamics of a “PQ-controlled” DTL VSI transferring power from dc sources to an ac grid—not dc-voltage power ports built by DTL VSIs (see [18]). Therefore, dc voltage is externally controlled by other entities' control loops for the dc-voltage, that is why the word “converter” has not been used like what is in [18] and [19] and the word “inverter” has been adopted similar to [20]. Moreover, two first-order low-pass filters are utilized in the control block diagram in order to remove the high-frequency switching noise. The inputs of those filters are V_{pcc_d} and V_{pcc_q} , and the outputs are V_d and V_q , respectively; the time constant of the filter employed is T as well.

Since the control structure uses two PI controllers in its most inner loops, two sets of dynamics are considered, which are expressed by (7) and (8). In this article, the DTL VSI works in active and reactive power control mode (i.e., PQ control). Consequently, the reference signals for active and reactive powers (P_{ref} and Q_{ref} in Fig. 4) generate the reference currents in the dq -frame (i.e., i_{1dref} and i_{1qref}). Therefore, one can obtain

$$\frac{dx_1}{dt} = I_{1dref} - I_{1d} \quad (7)$$

$$\frac{dx_2}{dt} = I_{1qref} - I_{1q} \quad (8)$$

where x_1 and x_2 are the states associated with two inner loop's PI controllers assigned to the d - and q -channels, respectively. As regards this, x_1 is the integrator outputs of the PI controllers assigned to the d -channel, and x_2 is that of the PI controllers assigned to the q -channel.

Since the average ac output voltage of the DTL VSI is proportional to the production of MI and dc voltage, V_{td} and V_{tq} are found as follows by considering Fig. 4:

$$V_{td} = K_{II}x_1 + K_{PI}I_{1dref} - K_{PI}I_{1d} + V_d - L\omega(t)I_{1q} + RI_{1d} \quad (9)$$

$$V_{tq} = K_{II}x_2 + K_{PI}I_{1qref} - K_{PI}I_{1q} + V_q + L\omega(t)I_{1d} + RI_{1q} \quad (10)$$

where K_{PI} and K_{II} are the proportional and integral coefficients of the current controllers, respectively.

B. PLL Dynamics

The linearized model of PLL is shown in Fig. 6. In practice, $H(s)$ can be any transfer function—which is able to stabilize the closed-loop dynamics shown in Fig. 6. However, in

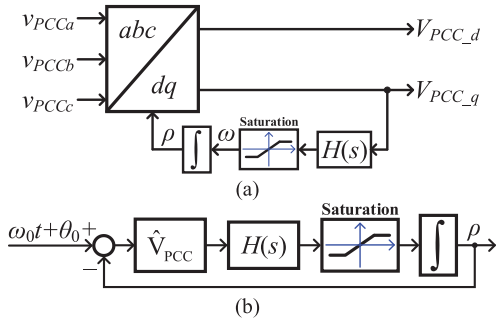


Fig. 6. (a) Implementation of PLL. (b) Linearized model of PLL.

this article, $H(s)$ is selected to be an industrially accepted controller, which is the proportional–integral–derivative (PID) controller described by (11) (see [19], [30], and the references therein)

$$H(s) = \frac{K_D s^2 + K_P s + K_I}{s} \quad (11)$$

where K_D , K_P , and K_I are derivative, proportional, and integral coefficients, respectively.

It is noteworthy that this analysis can easily be generalized to other types of PLL controllers. However, it needs related mathematical manipulations to find its state-space model—which is similar to the way performed for the PID controller here. For the state-space model of the PID controller, the “diagonal” canonical form is employed. As a result, the PLL state-space model is represented by

$$\frac{dx_{1\text{PID}}}{dt} = -\alpha x_{1\text{PID}} + V_{\text{PCC}_q} \quad (12)$$

$$\frac{dx_{2\text{PID}}}{dt} = -\beta x_{2\text{PID}} + V_{\text{PCC}_q} \quad (13)$$

where $x_{1\text{PID}}$ and $x_{2\text{PID}}$ are the states associated with two PLL PID controllers, and α and β are constants making the degree of the numerator of (11) equal to that of the denominator of (11)—thus making a “proper” transfer function. Thereby, it is possible to benefit from the diagonal canonical form of (11).

By using a diagonal canonical form, the angular frequency (ω) and phase angle (ρ) generated by the PLL are as follows:

$$\frac{d\rho}{dt} = \omega(t) = C_1 x_{1\text{PID}} + C_2 x_{2\text{PID}} + \frac{K_D}{\beta} V_{\text{PCC}_q} \quad (14)$$

where C_1 and C_2 are achieved from

$$C_1 = \left. \frac{K_D s^2 + K_P s + K_I}{\beta s + 1} \right|_{s=-\alpha} \quad (15)$$

$$C_2 = \left. \frac{\frac{K_P}{\beta} s^2 + \frac{K_P}{\beta} s + \frac{K_I}{\beta}}{s + \alpha} \right|_{s=-\frac{1}{\beta}}. \quad (16)$$

C. State-Space Model of Grid-Connected DTL VSIs

For evaluating the stability of the grid-connected DTL VSI, the linearized state-space model of the system is obtained.

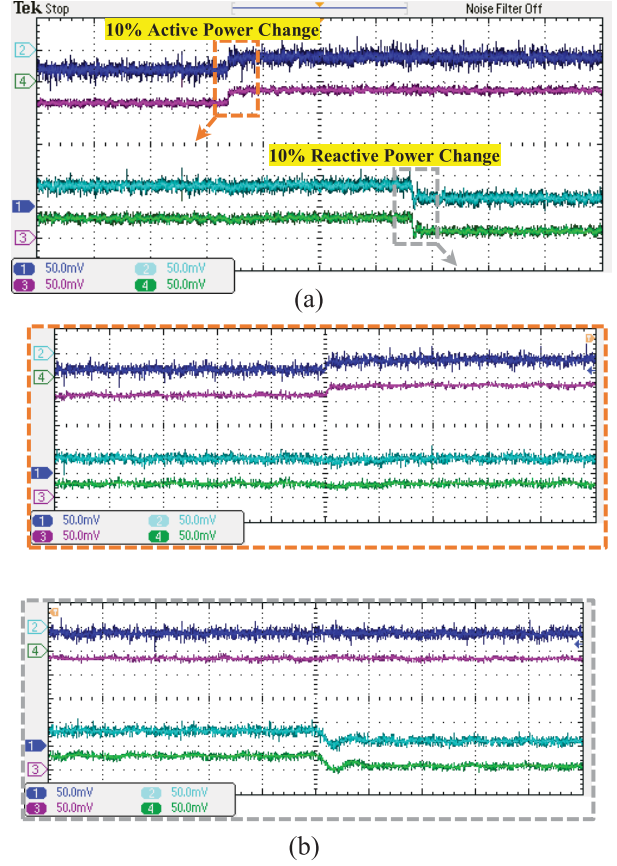


Fig. 7. Linearized state-space model validation of the DTL VSI by comparing the results of the linearized model and the response of experimental setup detailed in Section V-A. (a) Whole picture (200 ms/div) and (b) enlarged view of part (40 ms/div) (a), showing I_{1d} (Channel 1 in dark blue for the experiments and Channel 3 in dark magenta for the linearized model with 2.12 A/div) and I_{1q} (Channel 2 in cyan for the experiments and Channel 4 in lawn green for the linearized model with 2.12 A/div)—V/div of each channel has been shown at the bottom-left corner for all variables in pu.

In this regard, all nonlinear equations are linearized around the given operating point and arranged in the form of $\Delta \dot{X} = A \Delta X + B \Delta U$. Therefore, the linear state-space model of the grid-connected DTL VSI is given in (17), as shown at the bottom of the next page. It is in the form of $\Delta \dot{X} = A \Delta X + B \Delta U$ —in which the state and input matrices, i.e., A and B , are equal to $M^{-1} A_d$, and $M^{-1} B_d$.

In (17), M , A_{d11} , A_{d12} , A_{d21} , and A_{d22} are formulated by (A1)–(A5) in the Appendix. In (A1)–(A5), Δ with “small letters” shows the small-signal variation of the related variables, the subscript “0” denotes the equilibrium point of the corresponding state variable, $V_{\text{LL-rms}}$ is the line-to-line rms voltage of the grid, and α_0 is the phase difference between steady-state sinusoidal space phasors \vec{v}_{PCC} and \vec{v}_s .

The linearized model has been validated by comparing its time-domain simulation with that of nonlinear switching experiments. For doing the model verification, a 10% increase in active power and reactive power reference signals has been applied separately, while the DTL VSI’s operating point is 0.33/0.33 per unit (pu). Figs. 7 and 8 show the aforementioned validation results—the scaled-down test rig used for model validation in Figs. 7 and 8 has been thoroughly described

in Section V-A. The whole signals of V_{PCC_d} and V_{PCC_q} have been shown in Fig. 8(a), and in order to be able to demonstrate the dynamic performance of Fig. 8(a) accurately, its dc signal has been removed in Fig. 8(b).

D. State-Space Model of Grid-Connected TL VSIs

For comparing the grid-connected DTL VSI with a conventional system containing TL VSIs, the linearized model of the grid-connected two-level VSI (grid-connected TL VSI) is derived. Although a similar control block diagram can be used for both inverter structures, for grid-connected TL VSI, the control block diagram should generate pulses only for one VSI. As a result, the 180° shifter is omitted (see Fig. 4). Furthermore, the equivalent circuit is completely different for the grid-connected TL VSI. This circuit is shown in Fig. 9. Based on the equations obtained from Fig. 9, the linearized state-space model of the grid-connected TL VSI is described by (18), as shown at the bottom of this page. Similar to the DTL VSI, the state matrix of (18) consists of four matrices. It is noteworthy that two matrices—i.e., A_{t11} and A_{t12} —are not equal to A_{d11} and A_{d12} ; however, two other matrices named A_{t21} and A_{t22} are exactly analogous to their counterparts in A_d , which are termed A_{d21} and A_{d22} . A_{t11} and A_{t12} are expressed by (A6) and (A7) in the Appendix, respectively. Moreover, the matrix N is exactly the same as its counterpart

in (17), which is termed M . Note that, in (18) and (A1)–(A8) in the Appendix, Δ , the subscript “0,” V_m , and α_0 are the same as those defined in (A1)–(A5).

The linearized model of (18) has been validated by comparing its time-domain simulation with that of nonlinear switching experiments. For doing the model verification, a 10% increase in active power and reactive power reference signals has been applied, while the DTL VSI’s operating point is 0.33/0.33 pu. Figs. 10 and 11 show the aforementioned validation results—the scaled-down test rig used for model validation in Figs. 10 and 11 has been thoroughly described in Section V-A. The whole signals of V_{PCC_d} and V_{PCC_q} have been shown in Fig. 11(a), and in order to be able to demonstrate the dynamic performance of Fig. 11(a) accurately, its dc signal has been removed in Fig. 11(b).

E. Eigenvalue Analysis and Sensitivity Analysis

The closed-loop system’s eigenvalues representing all states are found by (17)—for the system formed by a DTL VSI—and by (18)—for the system formed by a TL VSI. A sensitivity analysis is performed when the SCCR is changed from 10 (whose resulting eigenvalues are shown by green “downward-pointing triangles”) to 1 (whose resulting eigenvalues are shown by red downward-pointing triangles) for both cases of DTL VSI and TL VSI—as it is

$$\begin{bmatrix} \Delta\dot{x}_1 \\ \Delta\dot{x}_2 \\ \Delta\dot{i}_{1d} \\ \Delta\dot{i}_{1q} \\ \Delta\dot{i}_{2d} \\ \Delta\dot{i}_{2q} \\ \Delta\dot{v}_{PCC_d} \\ \Delta\dot{v}_{PCC_q} \\ \Delta\dot{v}_d \\ \Delta\dot{v}_q \\ \Delta\dot{\rho} \\ \Delta\dot{x}_{1PID} \\ \Delta\dot{x}_{2PID} \end{bmatrix} = M^{-1} A_d \begin{bmatrix} \Delta x_1 \\ \Delta x_2 \\ \Delta i_{1d} \\ \Delta i_{1q} \\ \Delta i_{2d} \\ \Delta i_{2q} \\ \Delta v_{PCC_d} \\ \Delta v_{PCC_q} \\ \Delta v_d \\ \Delta v_q \\ \Delta \rho \\ \Delta x_{1PID} \\ \Delta x_{2PID} \end{bmatrix} + M^{-1} B_d \begin{bmatrix} i_{1dref} \\ i_{1qref} \end{bmatrix} = M^{-1} \begin{bmatrix} A_{d11} & A_{d12} \\ A_{d21} & A_{d22} \end{bmatrix} \begin{bmatrix} \Delta x_1 \\ \Delta x_2 \\ \Delta i_{1d} \\ \Delta i_{1q} \\ \Delta i_{2d} \\ \Delta i_{2q} \\ \Delta v_{PCC_d} \\ \Delta v_{PCC_q} \\ \Delta v_d \\ \Delta v_q \\ \Delta \rho \\ \Delta x_{1PID} \\ \Delta x_{2PID} \end{bmatrix} + M^{-1} \begin{bmatrix} 1 & 0 \\ 0 & 1 \\ 2K_{PI} & 0 \\ 0 & 2K_{PI} \\ 0 & 0 \\ 0 & 0 \\ 0 & 0 \\ 0 & 0 \\ 0 & 0 \\ 0 & 0 \\ 0 & 0 \\ 0 & 0 \end{bmatrix} \begin{bmatrix} i_{1dref} \\ i_{1qref} \end{bmatrix} \quad (17)$$

$$\begin{bmatrix} \Delta\dot{x}_1 \\ \Delta\dot{x}_2 \\ \Delta\dot{i}_{1d} \\ \Delta\dot{i}_{1q} \\ \Delta\dot{i}_{2d} \\ \Delta\dot{i}_{2q} \\ \Delta\dot{v}_{PCC_d} \\ \Delta\dot{v}_{PCC_q} \\ \Delta\dot{v}_d \\ \Delta\dot{v}_q \\ \Delta\dot{\rho} \\ \Delta\dot{x}_{1PID} \\ \Delta\dot{x}_{2PID} \end{bmatrix} = N^{-1} A_t \begin{bmatrix} \Delta x_1 \\ \Delta x_2 \\ \Delta i_{1d} \\ \Delta i_{1q} \\ \Delta i_{2d} \\ \Delta i_{2q} \\ \Delta v_{PCC_d} \\ \Delta v_{PCC_q} \\ \Delta v_d \\ \Delta v_q \\ \Delta \rho \\ \Delta x_{1PID} \\ \Delta x_{2PID} \end{bmatrix} + N^{-1} B_t \begin{bmatrix} i_{1dref} \\ i_{1qref} \end{bmatrix} = N^{-1} \begin{bmatrix} A_{t11} & A_{t12} \\ A_{t21} & A_{t22} \end{bmatrix} \begin{bmatrix} \Delta x_1 \\ \Delta x_2 \\ \Delta i_{1d} \\ \Delta i_{1q} \\ \Delta i_{2d} \\ \Delta i_{2q} \\ \Delta v_{PCC_d} \\ \Delta v_{PCC_q} \\ \Delta v_d \\ \Delta v_q \\ \Delta \rho \\ \Delta x_{1PID} \\ \Delta x_{2PID} \end{bmatrix} + N^{-1} \begin{bmatrix} 1 & 0 \\ 0 & 1 \\ K_{PI} & 0 \\ 0 & K_{PI} \\ 0 & 0 \\ 0 & 0 \\ 0 & 0 \\ 0 & 0 \\ 0 & 0 \\ 0 & 0 \\ 0 & 0 \\ 0 & 0 \end{bmatrix} \begin{bmatrix} i_{1dref} \\ i_{1qref} \end{bmatrix} \quad (18)$$

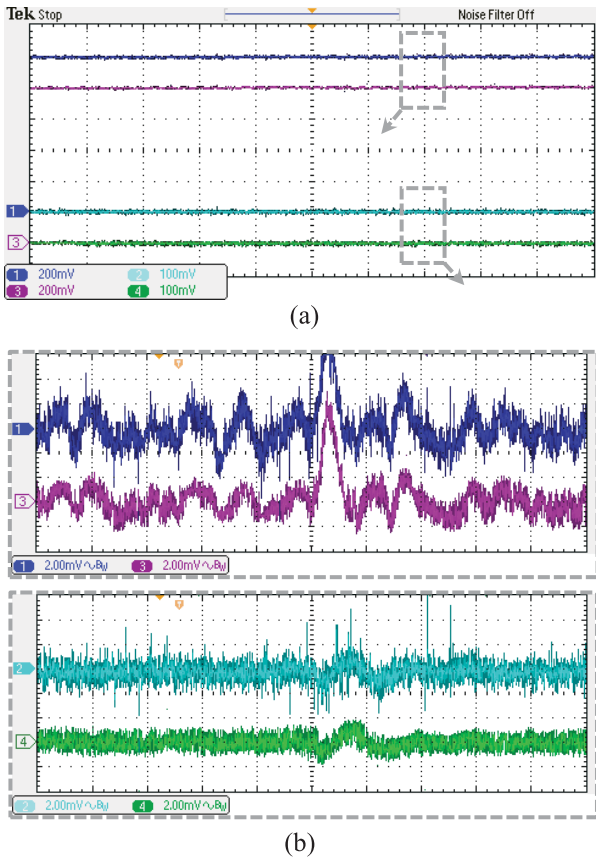


Fig. 8. Linearized state-space model validation of the DTL VSI by comparing the results of the linearized model and the response of experimental setup detailed in Section V-A. (a) Whole picture (200 ms/div), showing V_{PCC_d} (Channel 1 in dark blue for the experiments and Channel 3 in dark magenta for the linearized model with 33.96 V/div) and V_{PCC_q} (Channel 2 in cyan for the experiments and Channel 4 in lawn green for the linearized model with 33.96 V/div). (b) Enlarged view of the “ac signal” of (a) (0.34 V/div with 20 ms/div)—V/div of each channel has been shown at the bottom-left corner for all variables in pu.

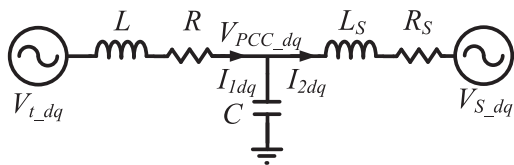


Fig. 9. Equivalent average model of the grid-connected TL VSI.

demonstrated in Figs. 12 and 13. For producing those simulations, the data in Table III in the Appendix have been used. In Figs. 12 and 13, the resulting eigenvalues for $1 < \text{SCCR} < 10$ are shown by blue “crosses.”

Therefore, the traces start with green downward-pointing triangles going to red downward-pointing triangles—associated with the SCCR, which varies from 10 to 1.

It is noteworthy that the controllers of both current loops and PLL have been synthesized with an adequate margin of stability criteria and acceptable performances. In this regard, by considering Fig. 6(b) and Table III in the Appendix and following the methods detailed in [18]–[20] and [30], it will be revealed that the PLL controller has induced 90° phase margin. Using the same data reveals that the time constants

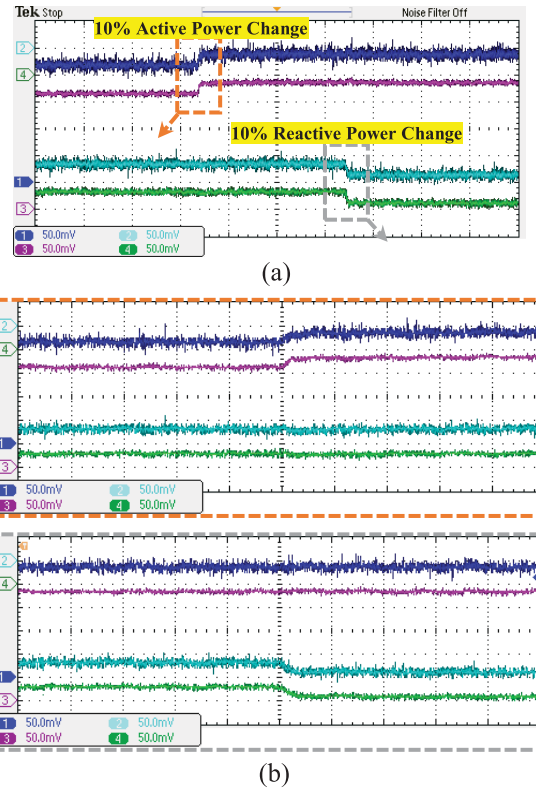


Fig. 10. Linearized state-space model validation of the DTL VSI by comparing the results of the linearized model and the response of experimental setup detailed in Section V-A. (a) Whole picture (200 ms/div) and (b) enlarged view of part (40 ms/div) (a), showing I_{1d} (Channel 1 in dark blue for the experiments and Channel 3 in dark magenta for the linearized model with 2.12 A/div) and I_{1q} (Channel 2 in cyan for the experiments and Channel 4 for the linearized model in lawn green with 2.12 A/div)—V/div of each channel has been shown at the bottom-left corner for all variables in pu.

τ_c of both structures have been set to 1 ms, thus resulting in the current closed-loop bandwidth of $\omega_c = 1/\tau_c = 1000$ rad/s. ω_c should be considerably smaller (i.e., ten times, which is almost 51 times in this article) than the switching frequency of the VSI (in rad/s)—which is an important requirement for PWM-based VSIs.

Comparing Figs. 12 and 13 reveals that the eigenvalues associated with the closed-loop system formed by the DTL VSI are further located in the left half-plane (LHP) with respect to the $j\omega$ -axis. Therefore, Figs. 12 and 13 have demonstrated that the closed-loop dynamic system formed by the DTL VSI is more stable than the closed-loop dynamic system formed by the TL VSI—since DTL VSI pushes the LHP closed-loop eigenvalues further left with respect to the $j\omega$ -axis. On top of the purely mathematical eigenvalue analysis, another rationale (which is based on the physics of the problem) is as follows. Indeed, the 180° phase shifter employed in generating voltages a' , b' , and c' of the VSI-2 in the DTL VSI (shown in Figs. 3 and 4) effectively and internally cancels some of the DTL VSI’s ac-side’s dynamics. This phenomenon does not happen in TL VSIs.

It should be pointed out that based on the abovementioned discussions, bad performances, instability, and eigenvalue variations will not be triggered by bad tuning of either the current

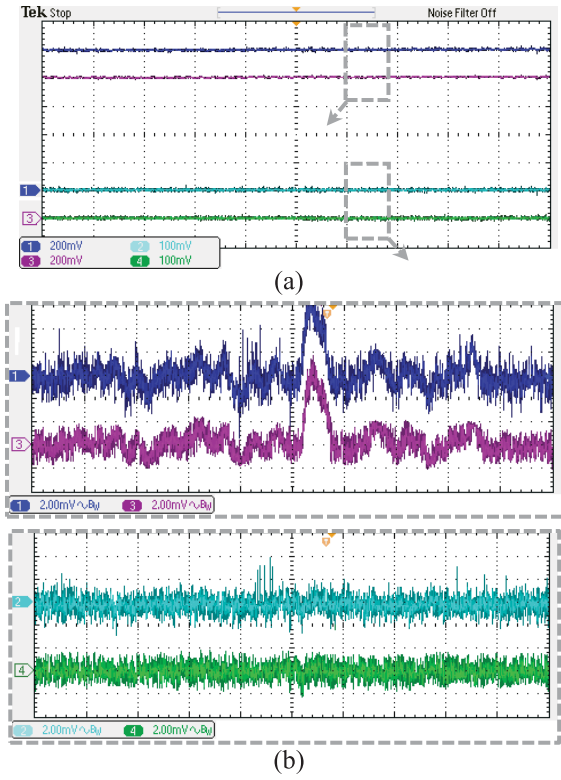


Fig. 11. Linearized state-space model validation of the DTL VSI by comparing the results of the linearized model and the response of experimental setup detailed in Section V-A. (a) Whole picture (200 ms/div), showing V_{PCC_d} (Channel 1 in dark blue for the experiments and Channel 3 in dark magenta for the linearized model with 33.96 V/div) and V_{PCC_q} (Channel 2 in cyan for the experiments and Channel 4 for the linearized model in lawn green with 33.96 V/div). (b) Enlarged view of only “ac signal” of (a) (0.34 V/div with 40 ms/div)—V/div of each channel has been shown at the bottom-left corner for all variables in pu.

control loops or the PLL; in this article, they are only coming from the ac grid impedance (regarded as grid weakness), which will be linked through PLL dynamics because all loops have been appropriately tuned in order to avoid “bad tuning problems.”

F. Boundaries of Stability Limit

For both DTL VSI and TL VSI, V_{t_dq} is connected to MI with the PWM nonlinear characteristic (see [31]). According to the nonlinear characteristic, in the linear region of $0 < MI < 1$, (\hat{V}/V_{dc}) is linearly varying concerning MI; however, for $MI > 1$, i.e., in overmodulation, (\hat{V}/V_{dc}) can only increase up to $4/\pi$ nonlinearly. For transferring a specific amount of

active power P and reactive power Q in equivalent circuits shown in Figs. 5 and 9, (\hat{V}/V_{dc}) is accordingly changed. Consequently, (\hat{V}/V_{dc}) is derived based on other parameters, such as P , Q , $V_{LL\text{-rms}}$ (secondary line-to-line rms voltage), V_{dc} , and the impedance of the system, i.e., z . By applying Kirchhoff’s voltage law (KVL), (19a) and (19b) shown at the bottom of this page are derived for calculating \hat{V}/V_{dc} based on other parameters of the related equivalent circuits, where z and θ are the magnitude and angle of the related impedance utilized between two sources containing the impedance of the filter and the grid for DTL VSI and TL VSI, respectively.

For different SCCR—ranging from 10 (for the strongest grid) to 1 (for the weakest grid) by changing R_S and L_S (all parameters are tabulated in Table III in the Appendix)—and for $P = 20$ kW and $Q = 20$ kvar, \hat{V}/V_{dc} of both structures has been shown in Fig. 14 by means of switching model (noted by “-S”) and equivalent circuit models (indicated by “-E”).

Based on Fig. 14, it can be seen that TL VSIs suffer from an inability to synthesize the voltage to transfer active and reactive powers at low SCCR because $\hat{V}/V_{dc} > 4/\pi$. In other words, for those SCCR, TL VSIs are not capable of synthesizing the required voltage. While the limit for TL VSI’s operation is SCCR = 3.6 based on the analysis of the equivalent circuit, this number for switching model is 2.6. The main reasons for this difference at lower SCCR are: 1) the PLL’s impact, which we cannot simply model and consider in the equivalent circuit, thereby playing a significant role at low SCCR; 2) the PWM nonlinear characteristic, which is not implementable in the equivalent circuit; and 3) the small amount of reactive power injected by the ac-side switching filter.

Last but not least, as shown earlier, the stability boundaries of the TL VSI has been met during the aforementioned range of operation, under which DTL VSI is controllable. In other words, the TL VSI is not even controllable under some of the range of operation. Section IV shows that Fig. 14 is valid and demonstrates that at SCCR = 2.6, TL VSI is not able to control active power and reactive power.

IV. SIMULATION RESULTS

The grid-connected DTL VSI shown in Fig. 2 is simulated in MATLAB Simulink in order to investigate the performance of this system. All required data have been tabulated in Table III in the Appendix and also explained here. The DTL VSI is connected to a 60-Hz, 260-V ac grid where the voltage is stepped up to 25 kV via an open-ended transformer with a turn ratio of 1:96.15. The short circuit ratio of the power network

$$\frac{1}{z^2}(V_{dc})^4 \left(\frac{\hat{V}}{V_{dc}} \right)^4 - \left[\frac{2P \cos \theta}{z} + \frac{2Q \sin \theta}{z} + \frac{(\sqrt{2} V_{LL\text{-rms}})^2}{z^2} \right] (V_{dc})^2 \left(\frac{\hat{V}}{V_{dc}} \right)^2 + (P^2 + Q^2) = 0, \quad \text{for DTL VSI} \quad (19a)$$

$$\frac{1}{z^2} \left(\frac{V_{dc}}{2} \right)^4 \left(\frac{\hat{V}}{V_{dc}} \right)^4 - \left[\frac{2P \cos \theta}{z} + \frac{2Q \sin \theta}{z} + \frac{\left(\sqrt{\frac{2}{3}} V_{LL\text{-rms}} \right)^2}{z^2} \right] \left(\frac{V_{dc}}{2} \right)^2 \left(\frac{\hat{V}}{V_{dc}} \right)^2 + (P^2 + Q^2) = 0, \quad \text{for TL VSI} \quad (19b)$$

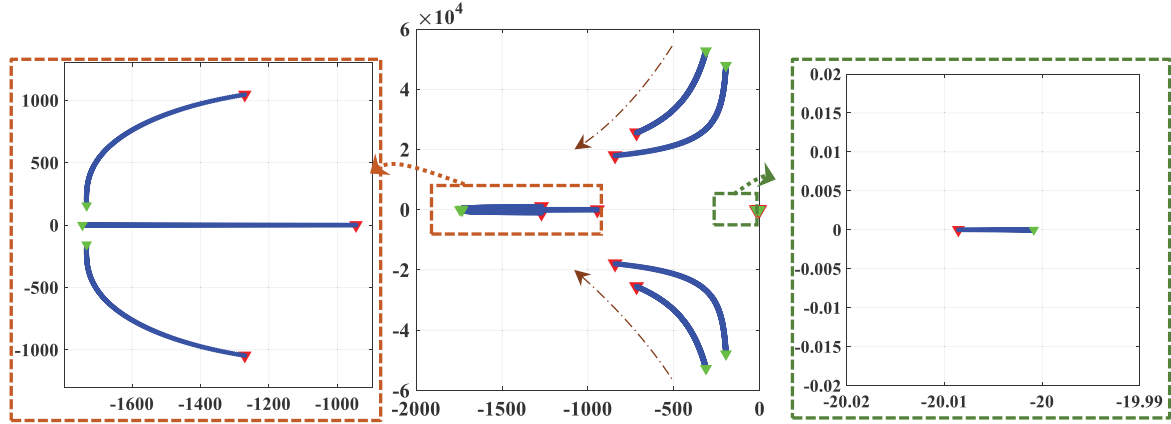


Fig. 12. Eigenvalue analysis associated with the DTL VSI—all eigenvalues including enlarged views.

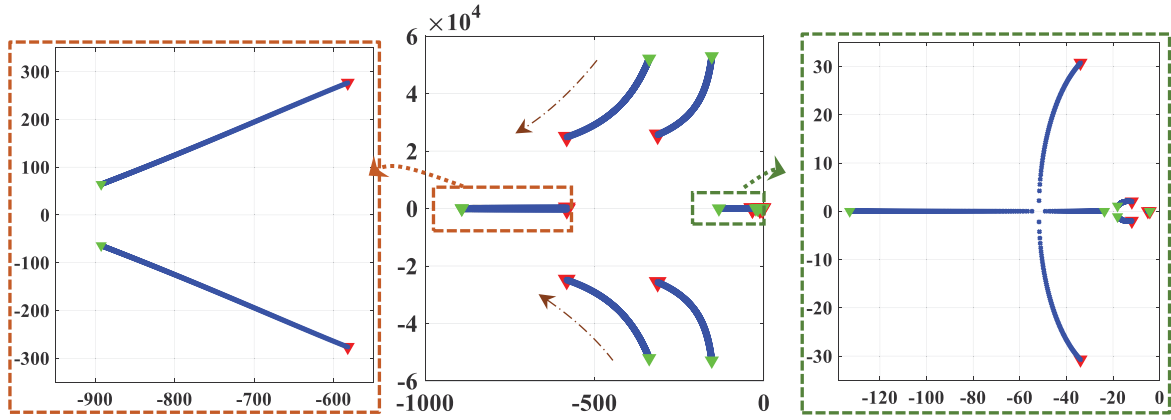


Fig. 13. Eigenvalue analysis associated with the TL VSI—all eigenvalues including enlarged views.

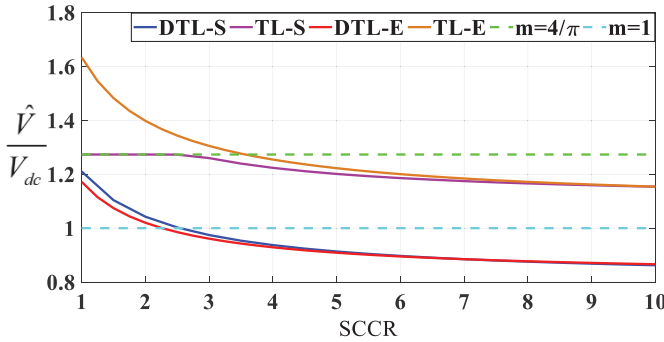


Fig. 14. \hat{V}/V_{dc} for different SCCR values associated with switching and equivalent models (for both DTL VSI and TL VSI).

at $\text{SCCR} = 1$ is equal to 30 kVA. The VSIs of DTL VSI are controlled separately with 8100-Hz switching frequency. Each VSI is connected to an isolated 500-V dc source. The current-controlled DTL VSI is shown in Fig. 4. For the ac-side filter, 2.4-mH inductance with 0.01- Ω resistance, as well as 1- μF capacitance, is utilized. It is noteworthy that in order to compare this system with the conventional ones, the grid-connected TL VSI is assumed and implemented in the same environment with similar parameters tabulated in Table III. Thus, the aforementioned VSI is connected to the same grid

(but with a regular $\text{Yd}1$ three-phase transformer in this case) with the turn ratio of 1:96.15—similar to that of the open-ended transformer in the DTL VSI case.

A. *PQ*-Controlled DTL VSI

The grid-connected DTL VSI's performances associated with tracking active/reactive power reference signals at different SCCR values are shown in Figs. 15 and 16. In Figs. 15 and 16, the reference signals have been shown by blue traces, and the output signals are depicted by red traces (for the proposed controller with the feedforward signals) and orange traces (for the controller without the feedforward signals). Orange traces indeed reveal that the feedforward in the proposed control is able to improve its performance—especially for the low SCCR values—by removing coupling signals.

From 0.0 to 0.5 s, the VSI has been set to inject 0 kW and 0 kvar so that all initial conditions' impacts on the simulation results diminish. Afterward, at 0.5 s, the active power reference changes from 0 to 10 kW; at 0.8 s, the reactive power reference varies from 0 to 10 kvar; at $t = 1.3$ s, the active power reference changes from 10 to 20 kW; and finally, at $t = 1.6$ s, the reactive power reference varies from 10 to 20 kvar—all by step functions. From Fig. 15, it is evident that not only at high SCCR values but also at very low SCCR values like $\text{SCCR} = 1.50$, the grid-connected DTL VSI is able to track the active

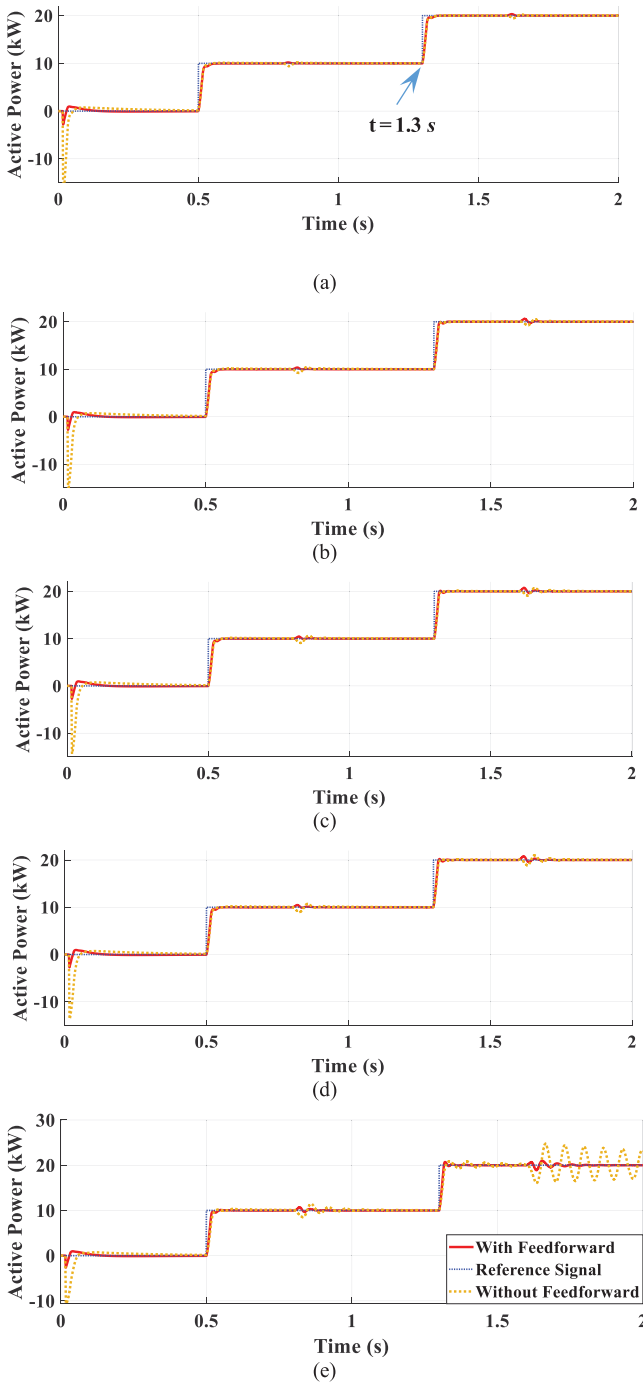


Fig. 15. Reference (blue trace) and actual value (red trace) of active powers delivered by grid-connected DTL VSI using the proposed controller with/without feedforward signals at (a) SCCR = 10, (b) SCCR = 4, (c) SCCR = 3, (d) SCCR = 2.6, and (e) SCCR = 1.50.

power reference. For $\text{SCCR} = 1$, it is also able to do so, but with more oscillations—for removing them, we can design separate controllers [19]. However, by a decrease in SCCR, the system needs more time to damp the generated oscillation after stepping up the reference values at $t = 1.3$ s and $t = 1.6$ s; this is because of having the eigenvalues that are more closed to the $j\omega$ -axis—for improving them, separate optimal controllers can be synthesized by separate research if required [19]. A similar response is also seen in Fig. 16.

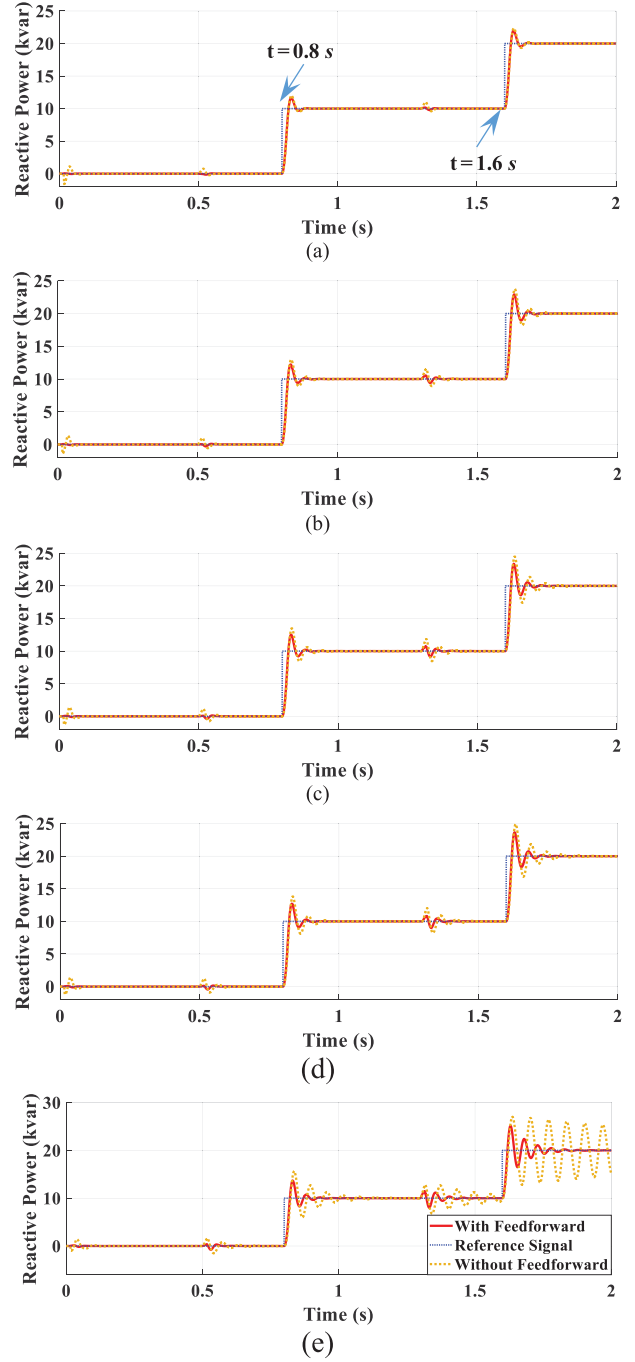


Fig. 16. Reference (blue trace) and actual value (red trace) of reactive powers delivered by the grid-connected DTL VSI using the proposed controller with/without feedforward signals at (a) SCCR = 10, (b) SCCR = 4, (c) SCCR = 3, (d) SCCR = 2.6, and (e) SCCR = 1.50.

The grid-connected DTL VSI is capable of responding to the reactive power demanded. Nevertheless, similar to Fig. 15, after any changes in reference values, the magnitude of the oscillation increases by decreasing the SCCR. At $\text{SCCR} = 1$, the highest oscillations in the active and reactive powers are observed. It can also be seen that at this SCCR with the highest reference values—i.e., at 20 kW and 20 kvar—the magnitude of the oscillations is intensified. As a result, the system requires 0.7 s to damp the oscillation and track the reference values perfectly.

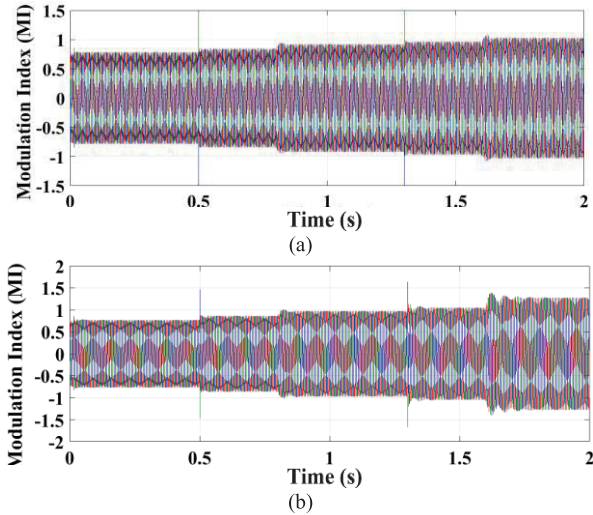


Fig. 17. MI for three phases (the rest of the phases use the 180° phase shifter shown in Fig. 4) at (a) SCCR = 2.6 and (b) SCCR = 1.5.

1) *Operation Without a Grid Fault*: Another factor that is essential to assess the performance of the system is to determine when overmodulation happens during power control, while SCCR changes. In other words, in which range of the SCCR the controller generates an MI, which is higher than one so that it is able to provide the active/reactive power. For the system employing DTL VSI, it experiences overmodulation for SCCR between 1 and 2.6, notably when the apparent power is 28.3 kVA (20 kW and 20 kvar). The MI curves of grid-connected DTL VSI at SCCR = 1 and SCCR = 2.6 are demonstrated in Fig. 17. Based on Fig. 17, at SCCR = 2.6, the controller generates an MI, which is higher than one, when it needs to inject 28.4 kVA. Though, by a decrease in SCCR, for example at SCCR = 1, overmodulation occurs even for providing 22.36 kVA. For a lower amount of active/reactive power, at SCCR = 1, the controller produces an MI, which is approximately equal to 1 [referred to Fig. 17(a)].

2) *Operation With a Grid Fault*: To investigate the performance of the grid-connected DTL VSI in all aspects, the performance of this system in faulty grid conditions should be studied as well. Thereafter, a solid three-phase fault (i.e., short-circuit without any impedance) occurs at 1.1 s and is cleared after one cycle (i.e., 16.67 ms), while the DTL VSI's active power and reactive power have been set to 20 kW and 20 kvar for $t < 1.1$ s, respectively. For short-circuit evaluation, the reference currents are limited to nominal currents in the dq -frame. The performances of the system at SCCR = 3, SCCR = 2, and SCCR = 1.78 are shown in Fig. 18. It can be seen that while the grid-connected DTL VSI shows stable performance at different SCCR in the normal condition, the stable performance after fault removal completely depends on the value of SCCR. For SCCR above 1.78, the system retrieves its stable performance; however, at SCCR lower than 1.78, the system does not track the reference values after fault removal.

Fig. 19 shows one of the phases' current (e.g., Phase "A" here) in the high-voltage side of the transformer for

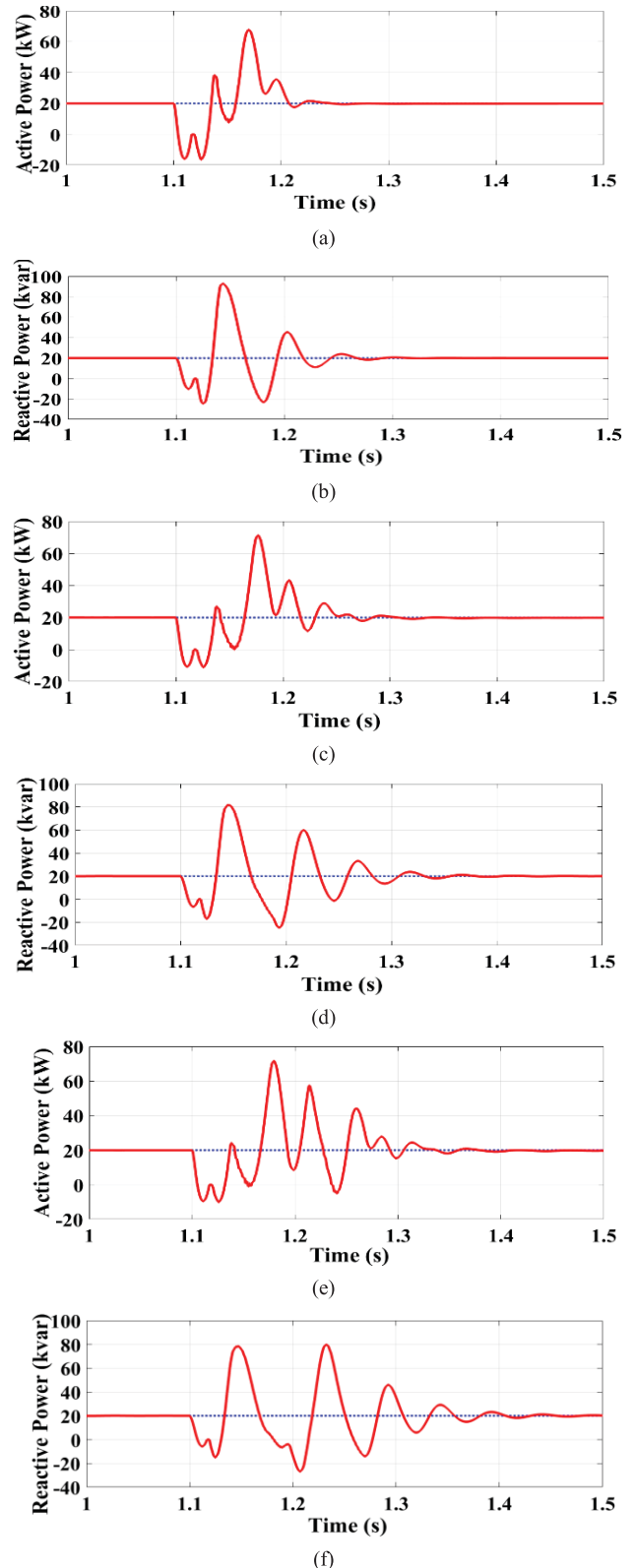


Fig. 18. Reference (blue trace) and actual value (red trace) of (a) active power at SCCR = 3, (b) reactive power at SCCR = 3, (c) active power at SCCR = 2, (d) reactive power at SCCR = 2, (e) active power at SCCR = 1.78, and (f) reactive power at SCCR = 1.78 for grid-connected DTL VSI.

SCCR = 5, 4, 3, and 1.78. According to Fig. 19, in the worst case scenario, i.e., SCCR = 1.78, the system needs about 0.25 s to recover its performance after a fault removal.

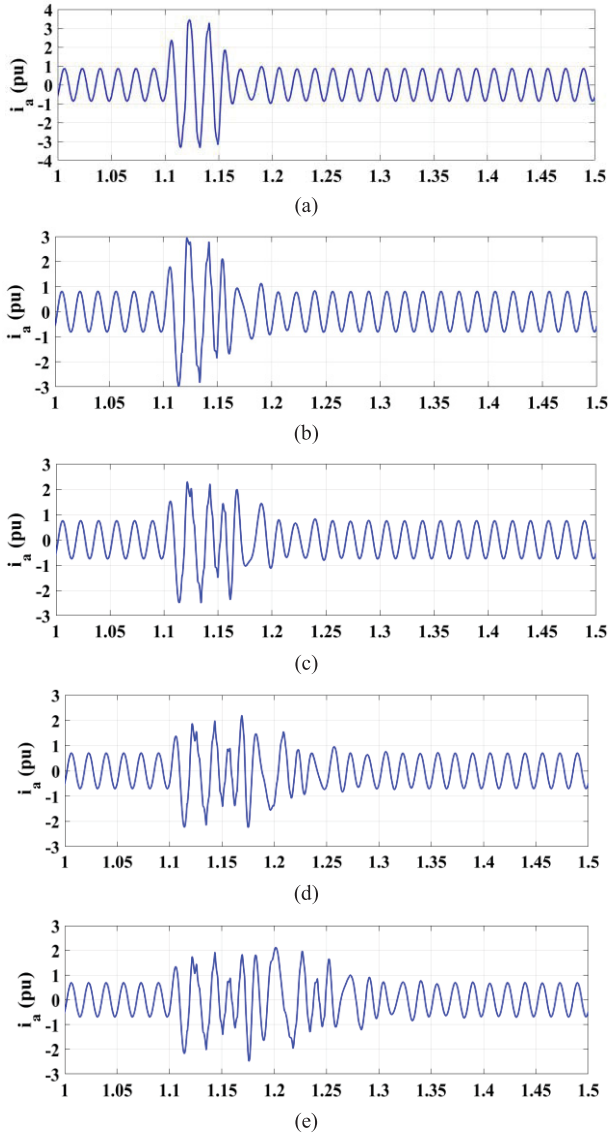


Fig. 19. Current of Phase A at high-voltage side of the open-ended transformer shown in Fig. 2. (a) SCCR = 5. (b) SCCR = 4. (c) SCCR = 3. (d) SCCR = 2. (e) SCCR = 1.78.

Indeed, $\text{SCCR} \geq 1.78$ is the exact range of SCCR in which stable performance after fault removal is achieved. It is noteworthy that the settings used here for the current controllers follow those of industrial converters because the amount of fault current (in pu) has been matched with that of practical cases during the same type of faults (see [32, Fig. 13])—subfigure of the section captioned “Bus 4; Top: Injected Current (kA).”

Also, just in case, the same simulations have been repeated for a five-cycle fault to check the performance of the system—although the five-cycle fault is not tolerable in practical power electronic systems. The simulations associated with the five-cycle fault have concluded that the aforementioned threshold has been calculated as $\text{SCCR} \geq 2.87$.

B. PQ-Controlled TL VSI

1) *Operation Without a Grid Fault*: In Figs. 20 and 21, the grid-connected TL VSI’s performance associated with

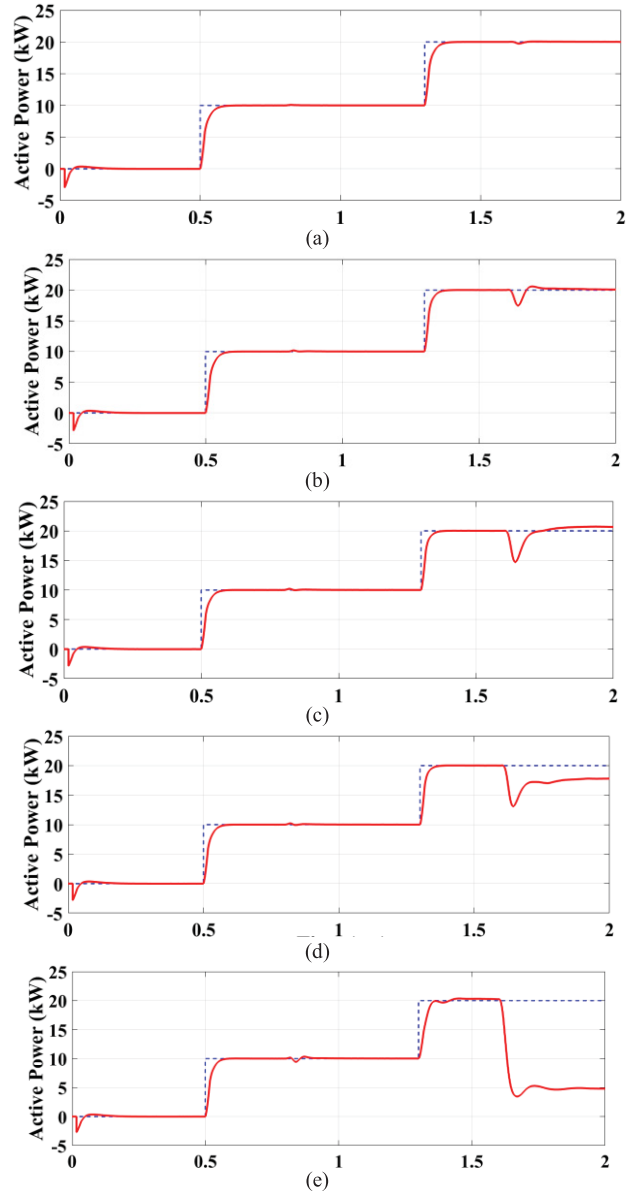


Fig. 20. Reference (blue trace) and actual value (red trace) of active powers by grid-connected TL VSI at (a) SCCR = 10, (b) SCCR = 4, (c) SCCR = 3, (d) SCCR = 2.6, and (e) SCCR = 1.50.

tracking active/reactive power reference signals at $\text{SCCR} = 10, 4, 3, 2.6$, and 1.50 is depicted. Similar to the case of grid-connected DTL VSI, the system should track the reference values. For SCCR higher than 2.6, the system is able to provide the demand even if at a lower value of SCCR, the system needs more time to damp the generated oscillations after experiencing a change in the references. However, at $\text{SCCR} \leq 2.6$, for reference power that equals 28.42 kW, the system is not able to generate 20 kW [referred to Fig. 20(c)]. The amount of generated active power at $\text{SCCR} = 2.6$ is equal to 17.9 kW. The lower the SCCR compared to 2.6, the lower the system ability to provide the active power. For example, at $\text{SCCR} = 1$ [referred to Fig. 20(d)], the system ability to provide the reference power is also reduced in comparison with when $\text{SCCR} = 2.6$. In case of $\text{SCCR} = 1$, the system is not capable of providing 20 kW

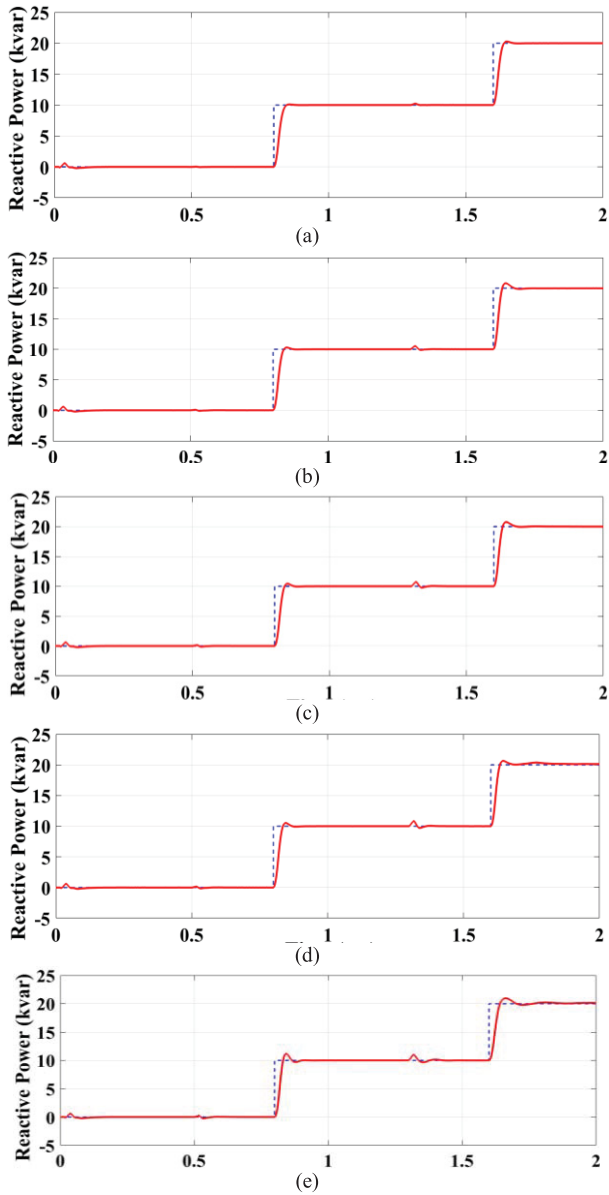


Fig. 21. Reference (blue trace) and actual value (red trace) of reactive powers by grid-connected TL VSI at (a) SCCR = 10, (b) SCCR = 4, (c) SCCR = 3, (d) SCCR = 2.6, and (e) SCCR = 1.50.

when the reactive power reference is 10 kvar (the apparent power reference is 22.36 kVA). It is noteworthy here that for any SCCR, the system is able to provide the reactive power reference. However, for the low SCCRs, the power capacity of the system is remarkably reduced because of the fact that the grid-connected TL VSI should be able to provide a significant amount of reactive power (which is the case in all VSCs' integration into weak grids).

For comparing both grid-connected inverters, the range of SCCR in which the grid-connected TL VSI controller generates MI higher than one is accordingly evaluated. Consequently, the MI curves of grid-connected TL VSI at SCCR = 10 and SCCR = 2.6 are shown in Fig. 22. Concerning Fig. 22, it can be seen that at SCCR = 10 and for lower values of the apparent power reference (lower than 28.42 kVA), the system benefits from operation in normal MI

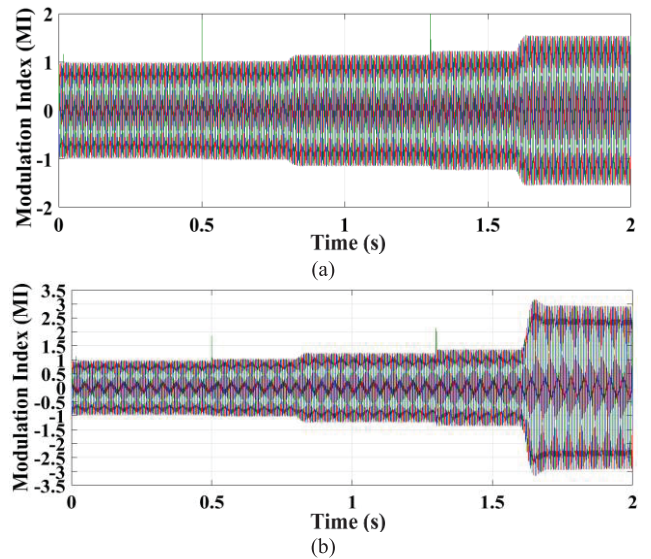


Fig. 22. MI at (a) SCCR = 10 and (b) SCCR = 2.6.

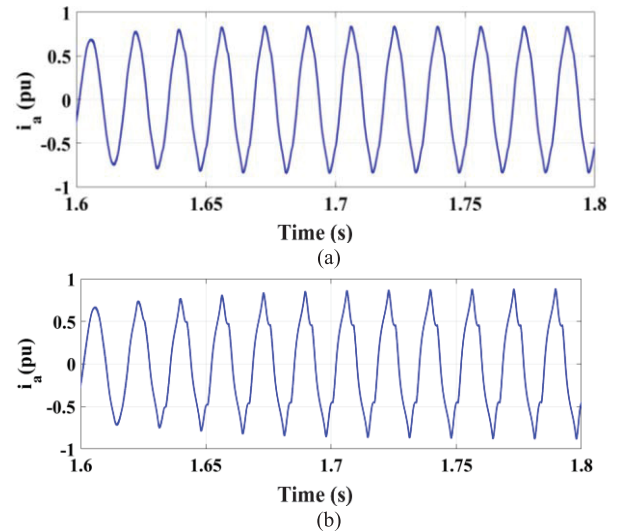


Fig. 23. Current of Phase A at (a) SCCR = 4 and (b) SCCR = 2.6.

range (i.e., without any overmodulations required). However, for the apparent power reference of 28.42 kVA, the system needs to employ overmodulation, thus suffering from its consequences. A similar response is obtained for SCCR = 2.6. The only difference is that the magnitude of MI should be increased when SCCR decreases from 10 to 2.6—the highest value of MI changes from 1.5 to around 3.

The Phase A current of the high-voltage side of the Yd1 three-phase transformer at SCCR = 4 and SCCR = 2.6 is presented in Fig. 23. According to Fig. 23, the associated current contains harmonics when the grid-connected TL VSI generates 28.42 kVA. The current THDs associated with SCCR = 4 and SCCR = 3 are equal to 4.22% and 11.42%, respectively. The corresponding values for grid-connected DTL VSI are less than 0.5%; for example, the current THD is 1.62% at SCCR = 1.5, hence getting much current THD in the much worse scenario. As a result, it has been demonstrated that not only does the grid-connected TL VSI suffer from

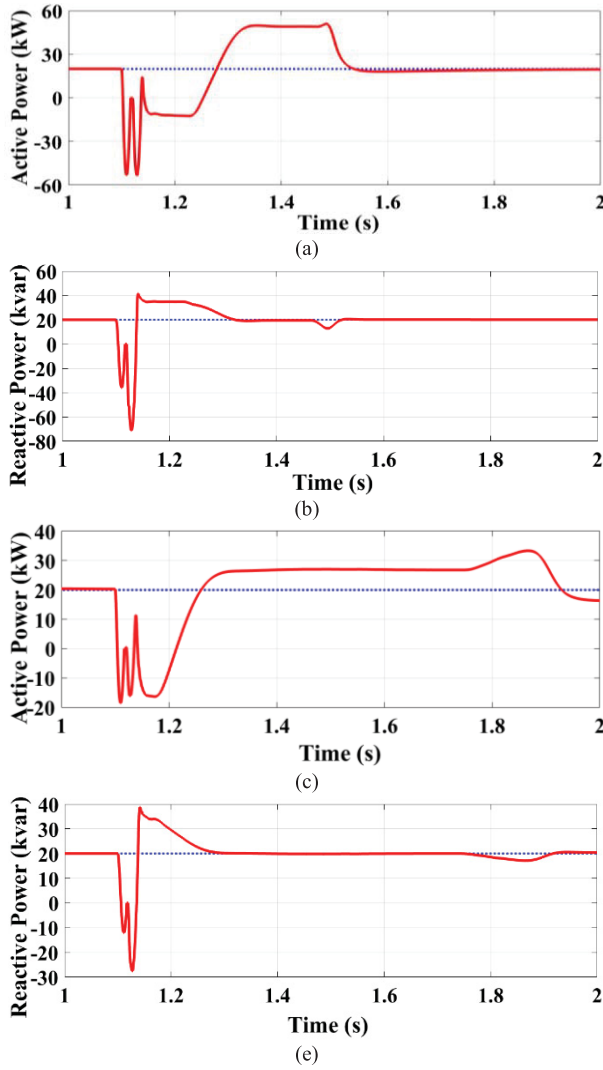


Fig. 24. Reference (blue trace) and actual value (red trace) of (a) active power at SCCR = 10, (b) reactive power at SCCR = 10, (c) active power at SCCR = 3.5, and (d) reactive power at SCCR = 3.5 for grid-connected TL VSI.

higher current THD compared to another one but also this problem worsens by a decrease in SCCR (lower than 4). Furthermore, this increase in the current THD is another effect showing that overmodulation dramatically happens and makes the performance weaker.

2) *Operation With a Grid Fault*: For comparing the two inverter structures, the performance of the grid-connected TL VSI in faulty grid conditions is also assessed. The same conditions as for the ones simulating the grid-connected DTL VSI's results are again considered here. The performance of the grid-connected TL VSI to track the reference values at different SCCR is shown in Fig. 24. According to Fig. 24(a) and (b), after fault removal, the controller of grid-connected TL VSI is able to obtain a stable performance after about 0.45 s. Albeit the system is able to track these reference signals after removing the fault, it should be considered that for SCCR = 10, the system needs about 0.45 s to track the references which compared to 0.15 s of the grid-connected DTL VSI, and the time required to reach stable performance is

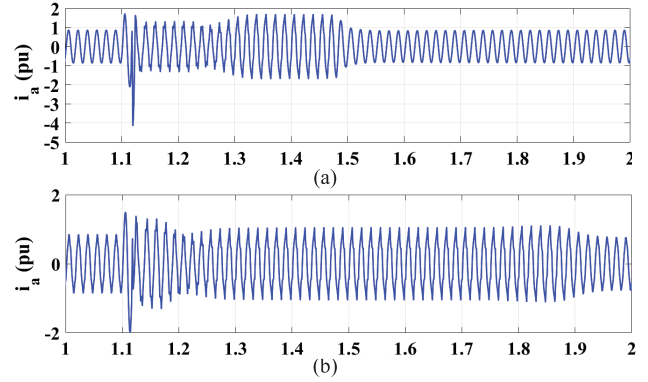


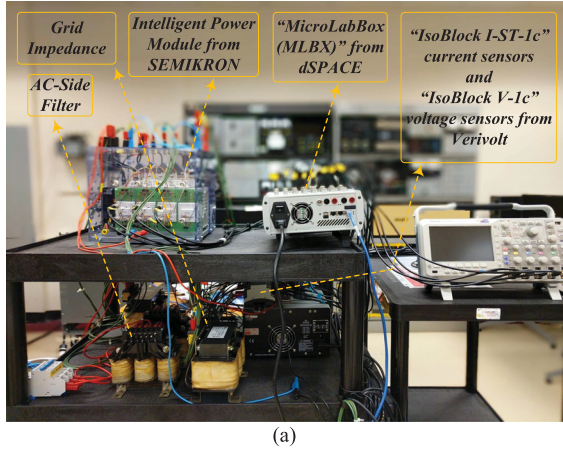
Fig. 25. Current of phase A at the high-voltage side of Yd1 transformer (a) SCCR = 10 and (b) SCCR = 3.5.

significantly extended. For the SCCR = 3.5, the system fails to provide the demand because although the reactive power reference is realized, the system is not able to generate the active one. The range of SCCR, in which the grid-connected TL VSI is able to stabilize active/reactive power demanded after the fault removal, is gained at $\text{SCCR} \geq 3.5$ —which is $\text{SCCR} \geq 1.78$ for DTL VSIs for comparison purposes. It concludes that DTL VSIs are able to operate desirably in a broader range.

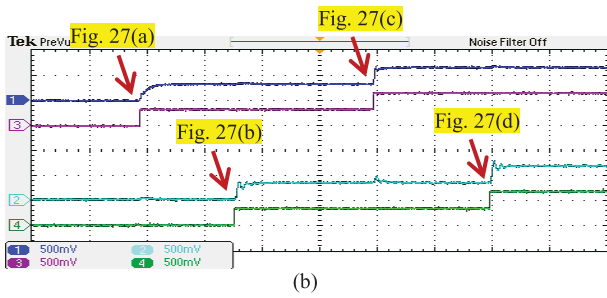
The fault currents of grid-connected TL VSI for SCCR = 3.5 and SCCR = 10 are shown in Fig. 25. Based on Fig. 25(a), at about $t = 1.5$ s, the system preserves a stable performance, which is similar to the case before fault happened, i.e., $t = 1.1$ s. However, for SCCR = 3.5—after fault removal—the current contains harmonics, showing that the controller is not able to recover its stable performance (even by synthesizing MI higher than 1).

V. EXPERIMENTAL RESULTS

For experimental evaluations, a scaled-down test rig, which is able to excite the dynamics of interest [18], [19], is being employed to emulate the dynamics of the grid-connected DTL VSI. It has been utilized for testing converter's performance when being used in the MMG's FIPES architecture. The experimental system consists of the VSI based on intelligent power modules from SEMIKRON, which includes insulated-gate bipolar transistors (IGBTs) built by "SKM 50 GB 123 D" modules, "SKHI 21A (R)" gate drives, and protection circuits. The switching frequency has been set to 8100 kHz. The ac-side filter inductance and resistance are 2.4 mH and 0.06 Ω , respectively, with an SCCR around 3. The dc-link capacitance and inductance are 2.04 mF and 1.50 mH, respectively. The three-phase converter is operated at 30 A and 208 V (line-to-line rms) and 400 V_{dc}—which have the ratio similar to that of the simulations. The converter's inductor currents and the voltages are measured by "IsoBlock I-ST-1c" current sensors and IsoBlock V-1c" voltage sensors from Verivolt, respectively. The converter is interfaced with a "MicroLabBox (MLBX)" from dSPACE. The proposed control algorithm is executed and run by a dual-core, 2-GHz "NXP (Freescale) QorIQ P5020" real-time processor. The PWM signals are generated by "Xilinx Kintex-7 XC7K325T" field-programmable



(a)



(b)

Fig. 26. (a) Some of the components used in the test rig and (b) snapshot of the experimental results associated with the “DTL VSI,” for the test cases similar to those in Figs. 15 and 16, showing active power and its reference signal (Channel 1 in dark blue for the measurement and Channel 3 in dark magenta for the reference signal of active power with 5.40 kW/div) and reactive power and its reference signal (Channel 2 in cyan for the measurement and Channel 4 in lawn green for the reference signal of reactive power with 5.40 kvar/div)—V/div of each channel has been shown at the bottom-left corner for all variables in pu with time horizontal axis 200 ms/div.

gate arrays (FPGAs) connected to digital inputs/outputs (I/Os). The MLBX interface board is equipped with eight 14-bit, 10-Msamples per second (Ms/s), differential analog-to-digital channels to interface the measured signals to the controller (with the functionality of free-running mode). The software code is generated by the Real-Time-WorkShop in the Simulink environment.

A. PQ-Controlled DTL VSI

The experiments have been conducted to replicate simulations as accurate as possible. In this regard, based on the available facilities and devices, the DTL VSI’s simulation results shown in Figs. 15 and 16 have been tested and duplicated. Here, Figs. 26 and 27 show the aforementioned experimental outcomes associated with the “DTL VSI.” All the results have been reported and generated in pu; $S_{\text{base-3phase}}$ for active/reactive power per unitization is 10.81 kVA, $I_{\text{base-peak}}$ for “peak” current per unitization is 42.43 A, and $I_{\text{base-rms}}$ for rms current per unitization is 30.00 A. In Fig. 26, Channels 1 and 2—with traces in dark blue and cyan colors—have been assigned to the measurements of active power and reactive power; Channels 3 and 4—with traces in dark magenta and lawn green colors—have been assigned to the reference signals of active power and reactive power, respectively. In Fig. 27, Channels 1 and 2 have been assigned

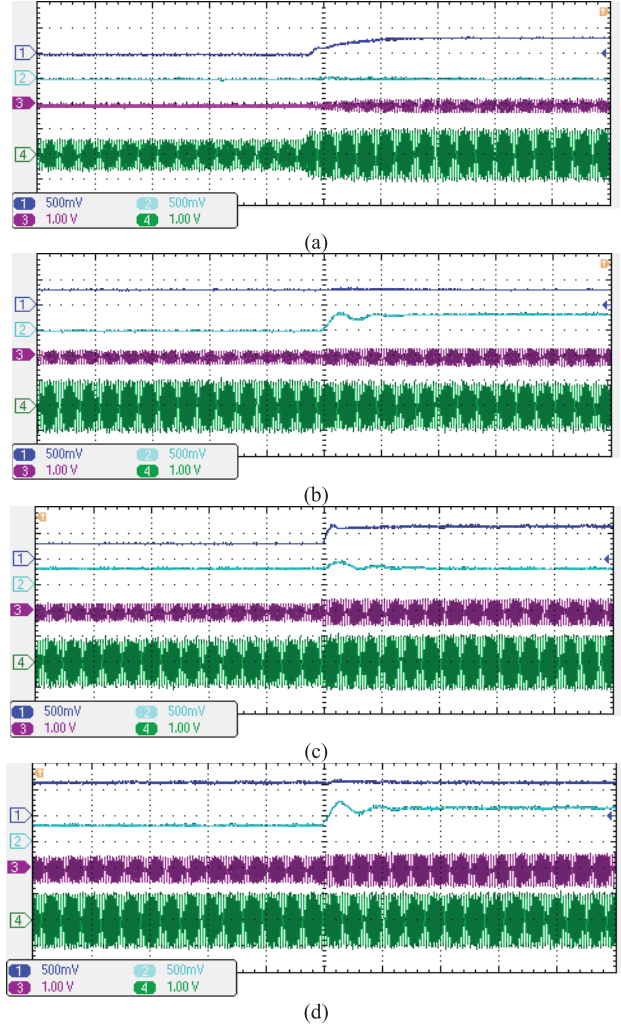


Fig. 27. Enlarged view of different parts and changes shown in Fig. 26. (a) Active power change, (b) reactive power change, (c) active power change, and (d) reactive power change with Phase A of the ac-side current (Channel 3 in dark magenta with 42.43 A/div) and the MI (Channel 4 in green with 1.00 V/div)—V/div of each channel has been shown at the bottom-left corner for all variables in pu with time horizontal axis 40 ms/div.

to the measurements of active power and reactive power; Channels 3 and 4 have been assigned to Phase A of the ac-side current and the related MI (as the main control input/lever), respectively. Similar to Figs. 15 and 16, after 0.00/-0.00-pu setpoints for active/reactive power, the first operating point is 0.33/-0.00-pu active/reactive power and, then, the test rig is set to 0.33/-0.33-pu active/reactive power; next, the third reference signal is 0.66-pu active power, while the reactive power is 0.33 pu; finally, the fourth one is 0.66-pu reactive power while the active power is 0.66 pu. Fig. 26 (including value per division of each channel) shows all test cases in one snapshot, and Fig. 27(a)–(e) shows the enlarged view of the aforementioned operating point changes shown in Fig. 26, respectively. In all figures, the volts per division (V/div) of each channel has been shown at the bottom-left corner. As they show, experiments are able to validate the simulations results of DTL VSI very well. For Fig. 26, Table I details the breakdown of power losses regarding different active/reactive power changes applied to the practical test rig.

TABLE I
BREAKDOWN OF POWER LOSSES IN FIGS. 26 AND 27

Component Loss \ Period	1 st Change	2 nd Change	3 rd Change	4 th Change
Total DC-Side Filter Loss in %	0.016	0.017	0.063	0.065
Total Converter Loss in %	0.48	0.65	1.05	1.31
Total AC-Side Filter Loss in %	0.099	0.17	0.37	0.53
Total Loss in %	0.60	0.83	1.48	1.91

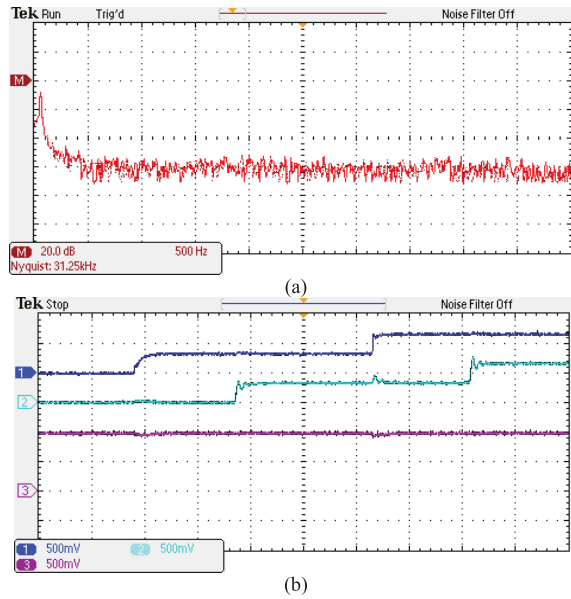


Fig. 28. (a) Frequency content of the ac-side current of Fig. 27 (20 dB per vertical division and 500 Hz per horizontal division) and (b) dynamic response of dc voltage of Fig. 26—showing active power (Channel 1 in dark blue with 5.40 kW/div), reactive power (Channel 2 in cyan with 5.40 kvar/div), and dc voltage (Channel 3 in dark magenta with 200 V/div)—V/div of each channel has been shown at the bottom-left corner for all variables in pu with time horizontal axis 200 ms/div.

Fig. 28(a) shows the power quality of the PQ-controlled DTL VSI under test using the fast Fourier transform (FFT). Because overmodulation does not happen here (shown in Fig. 27), the current has acceptable harmonic contents with the THD of 1.05%. In this test case, since DTL VSI needs to track different active/reactive power references as per ac grid's need, it should be able to work at various power factors (PFs). In Fig. 28(b), PF ranges from 0.71 to 1.00 based on the applied active/reactive power setpoints—similar to simulations results of Figs. 15 and 16. Fig. 28(b) also shows the dynamic response of dc voltage when the active/reactive power changes in Fig. 26.

B. PQ-Controlled TL VSI

For comparison, the test rig has also been reconfigured to the TL VSI architecture in this section—considering all requirements elaborated in Section IV. In this regard, the “TL VSI’s” simulation results shown in Figs. 20 and 21 have been tested and duplicated. Here, Fig. 29 (including value per division of each channel) and Fig. 30 show the

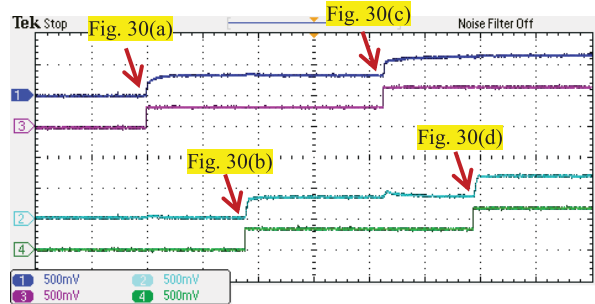


Fig. 29. Snapshot of the experimental results associated with the “TL VSI,” for the test cases similar to those in Figs. 20 and 21, showing active power and its reference signal (Channel 1 in dark blue for the measurement and Channel 3 in dark magenta for the reference signal of active power with 5.40 kW/div) and reactive power and its reference signal (Channel 2 in cyan for the measurement and Channel 4 in lawn green for the reference signal of reactive power with 5.40 kvar/div)—V/div of each channel has been shown at the bottom-left corner for all variables in pu with time horizontal axis 200 ms/div.

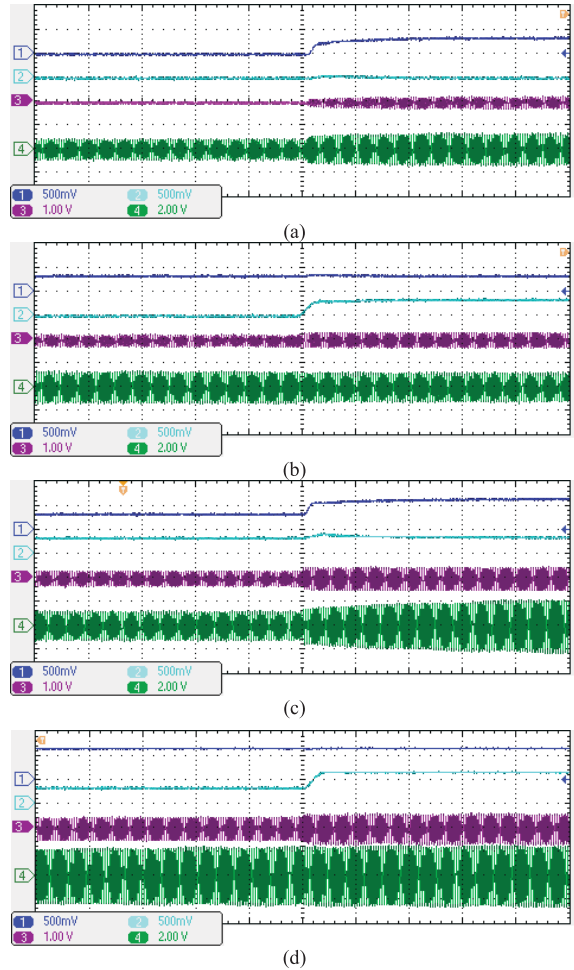


Fig. 30. Enlarged view of different parts and changes shown in Fig. 29. (a) Active power change, (b) reactive power change, (c) active power change, and (d) reactive power change with Phase A of the ac-side current (Channel 3 in dark magenta with 42.43 A/div) and the MI (Channel 4 in green with 2.00 V/div) with time horizontal axis 40 ms/div.

aforementioned experimental outcomes associated with the “TL VSI”—undergoing the same conditions and test cases used in Figs. 29 and 30. In all figures, the V/div of each channel has been shown at the bottom-left corner. They show that TL VSI is experiencing the overmodulation as predicated

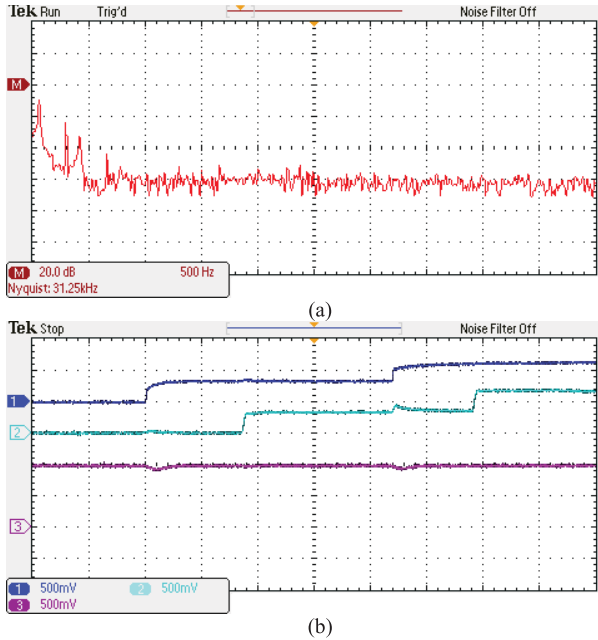


Fig. 31. (a) Frequency content of the ac-side current of Fig. 30 (20 dB per vertical division and 500 Hz per horizontal division) and (b) dynamic response of dc voltage of Fig. 29—showing active power (Channel 1 in dark blue with 5.40 kW/div), reactive power (Channel 2 in cyan with 5.40 kvar/div), and dc voltage (Channel 3 in dark magenta with 200 V/div)—V/div of each channel has been shown at the bottom-left corner for all variables in pu.

TABLE II
BREAKDOWN OF POWER LOSSES IN FIGS. 29 AND 30

Component Loss \ Period	1 st Change	2 nd Change	3 rd Change	4 th Change
Total DC-Side Filter Loss in %	0.029	0.030	0.12	0.13
Total Converter Loss in %	0.43	0.61	1.02	1.30
Total AC-Side Filter Loss in %	0.26	0.46	1.05	1.55
Total Loss in %	0.72	1.10	2.18	2.98

by simulations as well. Again, they are able to validate the simulation results of TL VSI. For Fig. 29, Table II details the breakdown of power losses regarding different active/reactive power changes applied to the experimental testbed.

Comparing Tables I and II shows that power losses are better in DTL VSIs. Also, Fig. 31(a) shows the power quality of the PQ-controlled TL VSI under test using FFT. Because overmodulation does happen here (shown in Fig. 30), the current has unwanted harmonic contents—especially for low-frequency harmonics—with the THD of 11.14%. In Fig. 31(b) [like Fig. 28(b)], PF ranges from 0.71 to 1.00 based on the applied active/reactive power setpoints—similar to simulations results of Figs. 20 and 21. Fig. 31(b) also shows the dynamic response of dc voltage when the active/reactive power changes in Fig. 26. It is noteworthy that there are always some practical uncertainties (which are frequent) in any experiments compared to simulations, especially when dealing with creating weak-grid conditions. Considering those uncertainties and simulation results in Section IV, experiments shown in Fig. 26–31 can genuinely demonstrate

TABLE III
PARAMETERS REQUIRED FOR FIGS. 2–25

Nominal rated power of the inverter, i.e., S_n for DTL VSI or TL VSI	30 kVA
Range of SCCR changes (with $R_s=2\pi f_s L_s$)	10.00 to 1.00
Secondary/primary nominal line-to-line rms voltage	260/25,000 V
Fundamental frequency f_s	60 Hz
Angular fundamental frequency ω_s	$2\pi \times 60$ rad/sec
Current controller gains K_p/K_H	2.4/10.0
LC-Filter inductance and total resistance (including the switch on-state resistance of r_{on})/capacitance	2.4 mH with 0.01 Ω /1.0 μ F
dc-link voltage	500 V
Switching frequency	8,100 Hz (\approx 50,894 rad/s)
Transformer ratio	1:96.15
PLL $K_p/K_i/K_D$ and time constant for derivative action	180/3200/1 and 1×10^{-4}
α and β	0.001/0.001

a good comparison between the performance of DTL VSI and that of the TL VSI very well.

VI. CONCLUSION

This article has revealed that DTL VSIs have been able to integrate dc sources into the future/present modernized FIPESs using MIACDC architecture more effectively—compared to the conventional TL VSIs. For doing so, this article has investigated the stability of the grid-connected DTL VSIs. In order to assess the proposed structure's stability mathematically, a linearized state-space model of the system has been derived, validated, and compared with that of conventional grid-connected TL VSI. In the aforementioned linearized models, the effects of both PLL and grid parameters on the whole dynamic system have been investigated. The theoretical analyses, simulation results, and experiments are able to verify the significant advantages of the grid-connected DTL VSI over the grid-connected TL VSI regarding stability and ability to operate in a broader range of the grid weakness. The salient benefits of employing a grid-connected DTL VSI in the MIACDC architecture of the future/present FIPES—instead of using a conventional TL VSI—have concluded as follows.

- 1) While the proposed PQ-controlled DTL VSI could track the reference powers for any value of SCCR, even at SCCR = 1, the grid-connected TL VSI failed to demonstrate a stable performance in a broad range of SCRRs and becomes unstable for SCRR lower than 2.6.
- 2) The power quality of the PQ-controlled DTL VSI is higher than that of TL VSI for the same grid condition.
- 3) The proposed grid-connected DTL VSI showed better transient performance to preserve the stability after fault removal. While SCRR = 1.78 was the lowest value that the grid-connected DTL VSI was able to retrieve its stable performance after removal of the one-cycle fault, the grid-connected TL VSI was not able to preserve and obtain its appropriate performance even for SCRR = 3.5 (for a one-cycle, solid, three-phase fault). Similarly, for faults with the other number of cycles, the DTL VSI showed better transients to preserve the stability after fault removal for lower SCRRs compared to those of the TL VSI.

$$M = \begin{bmatrix} 1 & 0 & 0 & 0 & 0 & 0 & 0 & 0 & 0 & 0 & 0 & 0 & 0 & 0 \\ 0 & 1 & 0 & 0 & 0 & 0 & 0 & 0 & 0 & 0 & 0 & 0 & 0 & 0 \\ 0 & 0 & L & 0 & 0 & 0 & 0 & 0 & 0 & 0 & 0 & 0 & 0 & 0 \\ 0 & 0 & 0 & L & 0 & 0 & 0 & 0 & 0 & 0 & 0 & 0 & 0 & 0 \\ 0 & 0 & 0 & 0 & L_S & 0 & 0 & 0 & 0 & 0 & 0 & 0 & 0 & 0 \\ 0 & 0 & 0 & 0 & 0 & L_S & 0 & 0 & 0 & 0 & 0 & 0 & 0 & 0 \\ 0 & 0 & 0 & 0 & 0 & 0 & C & 0 & 0 & 0 & 0 & 0 & 0 & 0 \\ 0 & 0 & 0 & 0 & 0 & 0 & 0 & C & 0 & 0 & 0 & 0 & 0 & 0 \\ 0 & 0 & 0 & 0 & 0 & 0 & 0 & 0 & 1 & 0 & 0 & 0 & 0 & 0 \\ 0 & 0 & 0 & 0 & 0 & 0 & 0 & 0 & 0 & 1 & 0 & 0 & 0 & 0 \\ 0 & 0 & 0 & 0 & 0 & 0 & 0 & 0 & 0 & 0 & 1 & 0 & 0 & 0 \\ 0 & 0 & 0 & 0 & 0 & 0 & 0 & 0 & 0 & 0 & 0 & 1 & 0 & 0 \\ 0 & 0 & 0 & 0 & 0 & 0 & 0 & 0 & 0 & 0 & 0 & 0 & 1 & 0 \\ 0 & 0 & 0 & 0 & 0 & 0 & 0 & 0 & 0 & 0 & 0 & 0 & 0 & 1 \end{bmatrix} \quad (A1)$$

$$A_{d11} = \begin{bmatrix} 0 & 0 & -1 & 0 & 0 & 0 & 0 \\ 0 & 0 & 0 & -1 & 0 & 0 & 0 \\ 2K_{II} & 0 & (R - 2K_{PI}) & -L \left(C_1 X_{1PID0} + C_2 X_{2PID0} + \frac{K_D}{\beta} V_{0-q0} \right) & 0 & 0 & -1 \\ 0 & 2K_{II} & L \left(C_1 X_{1PID0} + C_2 X_{2PID0} + \frac{K_D}{\beta} V_{PCC-q0} \right) & (R - 2K_{PI}) & 0 & 0 & 0 \\ 0 & 0 & 0 & 0 & -R_S & L_S \left(C_1 X_{1PID0} + C_2 X_{2PID0} + \frac{K_D}{\beta} V_{PCC-q0} \right) & 1 \\ 0 & 0 & 0 & 0 & 0 & -L_S \left(C_1 X_{1PID0} + C_2 X_{2PID0} + \frac{K_D}{\beta} V_{PCC-q0} \right) & 0 \\ 0 & 0 & 1 & 0 & 0 & -1 & 0 \end{bmatrix} \quad (A2)$$

$$A_{d12} = \begin{bmatrix} 0 & 0 & 0 & 0 & 0 & 0 & 0 & 0 \\ 0 & 0 & 0 & 0 & 0 & 0 & 0 & 0 \\ -L \frac{K_D}{\beta} I_{1q0} & 2 & 0 & 0 & 0 & -LC_1 I_{1q0} & -LC_2 I_{1q0} \\ \left(L \frac{K_D}{\beta} I_{1d0} - 1 \right) & 0 & 2 & 0 & 0 & LC_1 I_{1d0} & LC_2 I_{1d0} \\ L_S \frac{K_D}{\beta} I_{2q0} & 0 & 0 & -\sqrt{\frac{2}{3}} V_{LL-\text{rms}} \sin(\alpha_0) & L_S C_1 I_{2q0} & L_S C_2 I_{2q0} \\ \left(1 - L_S \frac{K_D}{\beta} I_{2d0} \right) & 0 & 0 & \sqrt{\frac{2}{3}} V_{LL-\text{rms}} \cos(\alpha_0) & -L_S C_1 I_{2d0} & -L_S C_2 I_{2d0} \\ C \left(C_1 X_{1PID0} + C_2 X_{2PID0} + 2 \frac{K_D}{\beta} V_{PCC-q0} \right) & 0 & 0 & 0 & CC_1 V_{PCC-q0} & CC_2 V_{PCC-q0} \end{bmatrix} \quad (A3)$$

$$A_{d21} = \begin{bmatrix} 0 & 0 & 0 & 1 & 0 & -1 & -C \left(C_1 X_{1PID0} + C_2 X_{2PID0} + \frac{K_D}{\beta} V_{PCC-q0} \right) & 1 \\ 0 & 0 & 0 & 0 & 0 & 0 & 0 & \frac{1}{T} \\ 0 & 0 & 0 & 0 & 0 & 0 & 0 & 0 \\ 0 & 0 & 0 & 0 & 0 & 0 & 0 & 0 \\ 0 & 0 & 0 & 0 & 0 & 0 & 0 & 0 \\ 0 & 0 & 0 & 0 & 0 & 0 & 0 & 0 \end{bmatrix} \quad (A4)$$

$$A_{d22} = \begin{bmatrix} -C \frac{K_D}{\beta} V_{PCC_d0} & 0 & 0 & 0 & -CC_1 V_{PCC_d0} & -CC_2 V_{PCC_d0} \\ 0 & -\frac{1}{T} & 0 & 0 & 0 & 0 \\ \frac{1}{T} & 0 & -\frac{1}{T} & 0 & 0 & 0 \\ \frac{K_D}{\beta} & 0 & 0 & 0 & C_1 & C_2 \\ 1 & 0 & 0 & 0 & -\alpha & 0 \\ 1 & 0 & 0 & 0 & 0 & -\beta \end{bmatrix} \quad (A5)$$

$$A_{t11} = \begin{bmatrix} 0 & 0 & -1 & 0 & 0 & 0 \\ 0 & 0 & 0 & -1 & 0 & 0 \\ K_{II} & 0 & -K_{PI} & 0 & 0 & 0 \\ 0 & K_{II} & 0 & -K_{PI} & 0 & -1 \\ 0 & 0 & 0 & 0 & -R_S & L_S \left(C_1 X_{1PID0} + C_2 X_{2PID0} + \frac{K_D}{\beta} V_{PCC_q0} \right) \\ 0 & 0 & 0 & 0 & -L_S \left(C_1 X_{1PID0} + C_2 X_{2PID0} + \frac{K_D}{\beta} V_{PCC_q0} \right) & -R_S \\ 0 & 0 & 1 & 0 & -1 & 0 \end{bmatrix} \quad (A6)$$

$$A_{t12} = \begin{bmatrix} 0 & 0 & 0 & 0 & 0 & 0 \\ 0 & 0 & 0 & 0 & 0 & 0 \\ 0 & 1 & 0 & 0 & 0 & 0 \\ -1 & 0 & 1 & 0 & 0 & 0 \\ L_S \frac{K_D}{\beta} I_{2q0} & 0 & 0 & -\sqrt{\frac{2}{3}} V_{LL\text{-rms}} \sin(\alpha_0) & L_S C_1 I_{2q0} & L_S C_2 I_{2q0} \\ \left(1 - L_S \frac{K_D}{\beta} I_{2d0} \right) & 0 & 0 & \sqrt{\frac{2}{3}} V_{LL\text{-rms}} \cos(\alpha_0) & -L_S C_1 I_{2d0} & -L_S C_2 I_{2d0} \\ C \left(C_1 X_{1PID0} + C_2 X_{2PID0} + 2 \frac{K_D}{\beta} V_{PCC_q0} \right) & 0 & 0 & 0 & C C_1 V_{PCC_q0} & C C_2 V_{PCC_q0} \end{bmatrix} \quad (A7)$$

$$A_{t21} = A_{d21}, \text{ and } A_{t22} = A_{d22} \quad (A8)$$

- 4) Only for the SCCR lower than 2.6, the controller of grid-connected DTL VSI dynamically generated an MI higher than 1 (i.e., having overmodulations during transients) in order to be able to generate the active/reactive power demanded. However, for the same system conditions and parameters, the stated overmodulation occurred even at SCCR = 10 when grid-connected TL VSI was utilized (while injecting 28.28 kVA for both of them).
- 5) While the current injected to the grid by DTL VSI had much fewer harmonics considering (i.e., 1.62% for SCCR = 1.5), the current of the grid-connected TL VSI contained significant harmonics even for higher values of the SCCR (i.e., 4.22% for SCCR = 4).

APPENDIX

See Table III; (A1)–(A4), shown at page 19; and (A5)–(A8), shown at the top of this page.

ACKNOWLEDGMENT

The authors would like to thank Verivolt Company for providing partial support to Georgia Southern University (<https://www.verivolt.com>) and dSPACE GmbH Company (<https://www.dspace.com/en/inc/home/products/hw/microlabbox.cfm>). This work has been done at Georgia Southern University (Statesboro Campus). The core program

of Energy, Power, Control, and Networks (EPCN) in the U.S. National Science Foundation's (NSF's) Division of Electrical, Communications and Cyber Systems (ECCS) has provided the awards.

REFERENCES

- [1] *IEEE Application Guide for IEEE Std 1547(TM), IEEE Standard for Interconnecting Distributed Resources With Electric Power Systems*, IEEE Standard 1547.2-2008, Apr. 2009, pp. 1–217.
- [2] Y. Yang, K. Zhou, H. Wang, F. Blaabjerg, D. Wang, and B. Zhang, "Frequency adaptive selective harmonic control for grid-connected inverters," *IEEE Trans. Power Electron.*, vol. 30, no. 7, pp. 3912–3924, Jul. 2015.
- [3] S. R. Pulikanti, G. Konstantinou, and V. G. Agelidis, "Hybrid seven-level cascaded active neutral-point-clamped-based multilevel converter under SHE-PWM," *IEEE Trans. Ind. Electron.*, vol. 60, no. 11, pp. 4794–4804, Nov. 2013.
- [4] P. Liu, S. Duan, C. Yao, and C. Chen, "A double modulation wave CBPWM strategy providing neutral-point voltage oscillation elimination and CMV reduction for three-level NPC inverters," *IEEE Trans. Ind. Electron.*, vol. 65, no. 1, pp. 16–26, Jan. 2018.
- [5] V. Khadkikar, D. Xu, and C. Cecati, "Emerging power quality problems and state-of-the-art solutions," *IEEE Trans. Ind. Electron.*, vol. 64, no. 1, pp. 761–763, Jan. 2017.
- [6] H. Stemmler and P. Guggenbach, "Configurations of high-power voltage source inverter drives," in *Proc. 5th Eur. Conf. Power Electron. Appl.*, Sep. 1993, pp. 7–14.
- [7] A. Edpuganti and A. K. Rathore, "New optimal pulsewidth modulation for single DC-link dual-inverter fed open-end stator winding induction motor drive," *IEEE Trans. Power Electron.*, vol. 30, no. 8, pp. 4386–4393, Aug. 2015.

- [8] K. K. Mohapatra, K. Gopakumar, V. T. Somasekhar, and L. Umanand, "A harmonic elimination and suppression scheme for an open-end winding induction motor drive," *IEEE Trans. Ind. Electron.*, vol. 50, no. 6, pp. 1187–1198, Dec. 2003.
- [9] A. Aghazadeh, M. Jafari, N. Khodabakhshi-Javinani, H. Nafisi, and H. J. Namvar, "Introduction and advantage of space opposite vectors modulation utilized in dual two-level inverters with isolated DC sources," *IEEE Trans. Ind. Electron.*, vol. 66, no. 10, pp. 7581–7591, Oct. 2019.
- [10] A. Aghazadeh, N. Khodabakhshi-Javinani, H. Nafisi, M. Davari, and E. Pouresmaeil, "Adapted near-state PWM for dual two-level inverters in order to reduce common-mode voltage and switching losses," *IET Power Electron.*, vol. 12, no. 4, pp. 676–685, Apr. 2019.
- [11] G. Grandi, C. Rossi, D. Ostoic, and D. Casadei, "A new multilevel conversion structure for grid-connected PV applications," *IEEE Trans. Ind. Electron.*, vol. 56, no. 11, pp. 4416–4426, Nov. 2009.
- [12] N. Kumar, T. K. Saha, and J. Dey, "Control, implementation, and analysis of a dual two-level photovoltaic inverter based on modified proportional-resonant controller," *IET Renew. Power Gener.*, vol. 12, no. 5, pp. 598–604, Apr. 2018.
- [13] N. Kumar, T. K. Saha, and J. Dey, "Sliding-mode control of PWM dual inverter-based grid-connected PV system: Modeling and performance analysis," *IEEE J. Emerg. Sel. Topics Power Electron.*, vol. 4, no. 2, pp. 435–444, Jun. 2016.
- [14] N. Kumar, T. K. Saha, and J. Dey, "Modeling, control and analysis of cascaded inverter based grid-connected photovoltaic system," *Int. J. Electr. Power Energy Syst.*, vol. 78, pp. 165–173, Jun. 2016.
- [15] R. Heydari, M. Gheisarnejad, M. H. Khooban, T. Dragicevic, and F. Blaabjerg, "Robust and fast voltage-source-converter (VSC) control for naval shipboard microgrids," *IEEE Trans. Power Electron.*, vol. 34, no. 9, pp. 8299–8303, Sep. 2019. [Online]. Available: <https://ieeexplore.ieee.org/document/8629975>
- [16] S. Peyghami, H. Mokhtari, and F. Blaabjerg, "Autonomous power management in LVDC microgrids based on a superimposed frequency droop," *IEEE Trans. Ind. Electron.*, vol. 33, no. 6, pp. 5341–5350, Jun. 2018.
- [17] I. U. Nutkani, L. Meegahapola, L. P. C. Andrew, and F. Blaabjerg, "Autonomous power management for interlinked AC-DC microgrids," *CSEE J. Power Energy Syst.*, vol. 4, no. 1, pp. 11–18, Mar. 2018.
- [18] M. Davari and Y. A.-R. I. Mohamed, "Robust multi-objective control of VSC-based DC-voltage power port in hybrid AC/DC multi-terminal micro-grids," *IEEE Trans. Smart Grid*, vol. 4, no. 3, pp. 1597–1612, Sep. 2013.
- [19] M. Davari and Y. A.-R. I. Mohamed, "Robust vector control of a very weak-grid-connected voltage-source converter considering the phase-locked loop dynamics," *IEEE Trans. Power Electron.*, vol. 32, no. 2, pp. 977–994, Feb. 2017.
- [20] S. Silwal, S. Taghizadeh, M. Karimi-Ghartemani, M. J. Hossain, and M. Davari, "An enhanced control system for single-phase inverters interfaced with weak and distorted grids," *IEEE Trans. Power Electron.*, vol. 34, no. 12, pp. 12538–12551, Dec. 2019. [Online]. Available: <https://ieeexplore.ieee.org/document/8682131>
- [21] S. Sang, N. Gao, X. Cai, and R. Li, "A novel power-voltage control strategy for the grid-tied inverter to raise the rated power injection level in a weak grid," *IEEE J. Emerg. Sel. Topics Power Electron.*, vol. 6, no. 1, pp. 219–232, Mar. 2018.
- [22] P. Mitra, L. Zhang, and L. Harnefors, "Offshore wind integration to a weak grid by VSC-HVDC links using power-synchronization control: A case study," *IEEE Trans. Power Del.*, vol. 29, no. 1, pp. 453–461, Feb. 2014.
- [23] A. Egea-Alvarez, S. Fekriasl, F. Hassan, and O. Gomis-Bellmunt, "Advanced vector control for voltage source converters connected to weak grids," *IEEE Trans. Power Syst.*, vol. 30, no. 6, pp. 3072–3081, Nov. 2015.
- [24] M. Durrant, H. Werner, and K. Abbott, "Model of a VSC HVDC terminal attached to a weak AC system," in *Proc. IEEE Conf. Control Appl.*, Istanbul, Turkey, Jun. 2003, pp. 178–182.
- [25] L. Zhang, L. Harnefors, and H.-P. Nee, "Power-synchronization control of grid-connected voltage-source converters," *IEEE Trans. Power Syst.*, vol. 25, no. 2, pp. 809–820, May 2010.
- [26] A. Golieva, "Low short-circuit ratio connection of wind power plants," M.S. thesis, Dept. Electr. Power Eng., Norwegian Univ. Sci. Technol. (NTNU), Trondheim, Norway, Aug. 2015.
- [27] D. Dong, B. Wen, D. Boroyevich, P. Mattavelli, and Y. Xue, "Analysis of phase-locked loop low-frequency stability in three-phase grid-connected power converters considering impedance interactions," *IEEE Trans. Ind. Electron.*, vol. 62, no. 1, pp. 310–321, Jan. 2015.
- [28] J. Z. Zhou, H. Ding, S. Fan, Y. Zhang, and A. M. Gole, "Impact of short-circuit ratio and phase-locked-loop parameters on the small-signal behavior of a VSC-HVDC converter," *IEEE Trans. Power Del.*, vol. 29, no. 5, pp. 2287–2296, Oct. 2014.
- [29] L. Harnefors, M. Bongiorno, and S. Lundberg, "Input-admittance calculation and shaping for controlled voltage-source converters," *IEEE Trans. Ind. Electron.*, vol. 54, no. 6, pp. 3323–3334, Dec. 2007.
- [30] A. Yazdani and R. Iravani, "Grid-imposed frequency VSC system: Control in dq-frame," in *Voltage-source Converters Power Systems*, 1st ed. Hoboken, NJ, USA: Wiley, 2010, ch. 8, sec. 4, pp. 217–223.
- [31] J. R. Espinoza, "Inverters," in *Power Electronics Handbook: Devices, Circuits, and Applications*, 3rd ed. Amsterdam, The Netherlands: Elsevier, 2011, ch. 15, sec. 2, pp. 359–361.
- [32] M. Davari and F. Katiraei, "Investigation and correction of phase shift delays in power hardware in loop real-time digital simulation testing of power electronic converters," in *Proc. Grid Future Symp. (CIGRE US Nat. Committee)*, Oct. 2015, pp. 1–11. [Online]. Available: <http://cigre-usnc.org/wp-content/uploads/2015/10/DAVARI.pdf>



Amir Aghazadeh was born in Tehran, Iran. He received the B.S. degree in electrical engineering from the Sadra Institute of Higher Education, Tehran, in 2010, and the M.S. degree in electrical engineering from the Amirkabir University of Technology (AUT), Tehran, in 2014. In 2013, he established the Golden Group (G2), implicating on emerging and selected topics in power electronics. He is currently with the Center of Excellence in Power Systems, Department of Electrical Engineering, Amirkabir University of Technology, Tehran, Iran. His research interests include power electronics and its application in power systems.



Masoud Davari (S'08–M'17–SM'19) was born in Isfahan, Iran, on September 14, 1985. He received the B.Sc. degree (Hons.) in electrical engineering–power from the Isfahan University of Technology, Isfahan, in September 2007, the M.Sc. degree (Hons.) in electrical engineering–power from the Amirkabir University of Technology–Tehran Polytechnic, Tehran, Iran, in January 2010, and the Ph.D. degree in electrical engineering–energy systems from the University of Alberta, Edmonton, AB, Canada, in January 2016.

He was with the Iran's Grid Secure Operation Research Center and Iran's Electric Power Research Institute (EPRI), Tehran, from January 2010 to December 2011. From April 2015 to June 2017, he has collaborated with Quanta-Technology Company, Markham, ON, Canada, in the field of the dynamic interaction of renewable energy systems with smart grids as well as control, protection, and automation of microgrids as a Senior Research and Development Specialist and Senior Consultant. In July 2017, he joined the Department of Electrical and Computer Engineering, Allen E. Paulson College of Engineering and Computing, Georgia Southern University, Statesboro, GA, USA, as a tenure-track Assistant Professor. He has developed and implemented several experimental test rigs for both research universities and the industry. He is also the author and the invited reviewer of several of the IEEE Transactions and Journals, IET journals, *Energies Journal*, and various IEEE conferences, and the invited speaker at different universities and diverse societies. His research interests include the dynamics, controls, and protections of different types of power electronic converters, which are employed in the hybrid ac/dc smart grids, and hardware-in-the-loop (HIL) testing of modernized power systems.

Dr. Davari is an invited member of the Golden Key International Honour Society. He has been an active member and the Chapter Lead (for Chapter 3) of the IEEE WG P2004, a newly established the IEEE working group on the hardware-in-the-loop (HIL) simulation for the IEEE Standards Association, since June 2017. He served as the Chair for the Literature Review Subgroup of DC@home Standards for the IEEE Standards Association from April 2014 to October 2015.



Hamed Nafisi was born in Tehran, Iran. He received the B.Sc., M.Sc., and Ph.D. degrees in electrical engineering from the Amirkabir University of Technology, Tehran, Iran, in 2006, 2008, and 2014, respectively.

He is currently an Assistant Professor with the Department of Electrical Engineering, Amirkabir University of Technology. His current research interests include smart grids, power system protection, and power electronics application in power systems.



Frede Blaabjerg (S'86–M'88–SM'97–F'03) received the Ph.D. degree in electrical engineering from Aalborg University, Aalborg, Denmark, in 1995.

He was with ABB-Scandia, Randers, Denmark, from 1987 to 1988. He became an Assistant Professor in 1992, an Associate Professor in 1996, and a Full Professor of power electronics and drives with the Department of Energy Technology, Aalborg University, in 1998, where he has become a Villum Investigator since 2017. He is the honoris causa at the University Politehnica Timisoara (UPT), Timisoara, Romania, and Tallinn Technical University (TTU), Tallinn, Estonia. He has published more than 600 journal articles in the fields of power electronics and its applications. He is the coauthor of four monographs and the editor of ten books in power electronics and its applications. His current research interests include power electronics and its applications, such as in wind turbines, photovoltaic systems, reliability, harmonics, and adjustable speed drives.

Dr. Blaabjerg received 31 IEEE Prize Paper Awards, the IEEE PELS Distinguished Service Award in 2009, the EPE-PEMC Council Award in 2010, the IEEE William E. Newell Power Electronics Award 2014, and the Villum Kann Rasmussen Research Award 2014. He was the recipient of the "Global Energy" award for significant contribution to the development of technologies that provide new opportunities in energy development in 2019. He is the President of the IEEE Power Electronics Society from 2019 to 2020 and Vice-President of the Danish Academy of Technical Sciences. He was the Editor-in-Chief of the IEEE TRANSACTIONS ON POWER ELECTRONICS from 2006 to 2012. He was a Distinguished Lecturer of the IEEE Power Electronics Society from 2005 to 2007 and the IEEE Industry Applications Society from 2010 to 2011 and 2017 to 2018. He was nominated in 2014–2018 by Thomson Reuters to be included in the 250 most cited researchers in engineering in the world.